Biphasic P3/O3 driven excellent electrochemical behavior and structural stability in a dual pillar-ions sodium layered oxide cathode

Neha Dagar¹, Samriddhi Saxena¹, Velaga Srihari², Himanshu Kumar Poswal², Sonia Deswal³, Pradeep Kumar³, and Sunil Kumar^{1,*}

¹Department of Metallurgical Engineering and Materials Science, Indian Institute of Technology Indore, Simrol, 453552, India

²High Pressure & Synchrotron Radiation Physics Division, Bhabha Atomic Research Centre, Mumbai, 400085, India

³School of Physical Sciences, Indian Institute of Technology Mandi, Mandi, 175005, India *sunil@iiti.ac.in

ABSTRACT

Layered oxides suffer from detrimental phase transformations during the charge-discharge process, limiting their long-term cyclability and causing poor rate performance as Na-ion battery cathodes. Herein, a Ti/Al co-doped Na_{2/3}Mn_{2/3}Ni_{1/3}O₂ cathode with an optimized P3/O3 biphasic structure is designed that effectively constrains these undesirable phase transformations and cooperative Jahn-Teller distortion. Ti/Al doping imparts excellent electrochemical properties with Na_{0.77}Mn_{0.47}Al_{0.10}Ti_{0.10}Ni_{0.33}O₂ (NMAT-10) shows an excellent specific capacity of ~175.5 mAh g⁻¹ at 0.1C in 1.5-4.2 V range and a capacity retention of 83% after 300 cycles at 2C in 2.0-4.2 V. It also exhibits a much-improved rate capability with about 80% capacity at 5C relative to the capacity observed at 0.1C. These improvements in electrochemical performance are attributed to the stronger Al-O bond, which suppresses the severity of P3↔P3'↔O3 phase transformation, as confirmed by the operando synchrotron x-ray diffraction studies. The practical viability of the NMAT-10 cathode is verified in a full cell using a commercial hard-carbon anode, which showed a discharge capacity of ~80 mAh g⁻¹ at 0.2C and a remarkable capacity retention of 86% after 100 cycles. This work highlights the P3/O3 biphasic structure as an effective approach to achieve an excellent rate performance and better cycling stability in layered oxides for sodium-ion batteries.

KEYWORDS: Na-ion batteries, P3/O3 biphasic cathode, *Operando* synchrotron XRD, Electrochemical behavior

1. INTRODUCTION

A global push towards carbon neutrality has made efficient energy storage systems a key focus of scientific research. Accordingly, rechargeable batteries have become indispensable in modern society due to their use in various applications [1]. Owing to their superior energy density and long-term cycling performance, lithium-ion batteries (LIBs) are the dominant electrochemical energy storage devices for electric vehicles and electronic device applications. However, the limited lithium reserves and the high cost associated with its supply are still major challenges [2, 3]. As a result of the similarity in operation and the widespread availability of raw precursor, high-performance Na-ion batteries (NIBs) can be used as an alternative to Liion batteries [4].

Within sodium-ion batteries, the cathode material is pivotal for energy density and cost. A wide range of materials is being investigated for their potential use as NIB cathodes, including layered oxides, polyanionic compounds, and Prussian blue analogs [5-7]. Layered Na-transition metal oxides (Na_xTMO₂), 0≤x≤1, TM is a redox-active transition metal like Mn, Fe, Ni, Co, or a combination of these, have a performance edge due to their high specific capacity and structural flexibility [8, 9]. Depending on the coordination geometry of the sodium site (either Prismatic - P or octahedral - O), layered oxides (LOs) can take on a variety of structural forms. P and O-type structures in layered oxides have advantages and disadvantages regarding cathode performance parameters [10, 11]. Due to the high Na content (x>0.8), O3 structures show a high specific capacity. At the same time, P2 and P3-type phases, because of the prismatic environment, offer faster Na-ion diffusion, leading to better rate performance [12-14]. In recent times, there has been a focus on biphasic (P2/O3, P3/O3, P2/P3) cathodes that show high specific capacity along with better rate capability [15-23].

The LOs (archetypical O3-NaMn_{0.5}Ni_{0.5}O₂ and P2-Na_{2/3}Mn_{2/3}Ni_{1/3}O₂) with Ni as the redoxactive cation show good specific capacity and rate capability as NIB cathode materials [15, 18, 24-29]. The Ni^{2+/3+/4+} redox process in these materials offers a high specific capacity and high voltage. The activation of Mn^{4+/3+} redox provides additional capacity (albeit at lower voltages) but tends to induce phase transitions as a consequence of the Jahn-Teller distortion. The irreversible phase transformations (P2 to O2 and O3 to P3) during charging and discharging cause structural degradation due to the volume change, leading to capacity fading with cycling [14, 30]. Among various strategies, doping with inactive cations has shown enhancement in the cycle life of layered oxide due to the crystal structure stabilization during the charge-discharge

process [25, 26, 28-36]. Ti-doping is a popular choice in this regard as it improves the rate performance, apart from cycle stability, by increasing the Na-O2 interlayer spacings in P2-type LOs [28, 30, 32, 37]. Al³⁺ doping (fixed oxidation state and strong electron exchange with oxygen) is also reported to be useful in improving the performance of layered oxide cathodes as Al-ions stabilize the matrix structure and effectively suppress the phase transformation [29, 34, 38]. For instance, 11.1% Al-doped Na_{2/3}MnO₃ cathode delivered an improved specific capacity of 162.3 mAh g⁻¹ at 0.1 C, as well as stable cycling performance with 83% capacity retention after 150 cycles in the potential window of 2.0–4.0 V [29]. The presence of Al³⁺ in tunnel-type Na_xMnO₂ has also been reported to be beneficial in improving cycle life [39]. As the redox inactive cations do not contribute to the specific capacity, the amount of such dopants in the crystal structure has a profound effect on the electrochemical properties and, therefore, should be carefully considered [33]. Further, the incorporation of multiple cations (including dual doping, ternary, and quaternary systems) at the transition metal site in layered oxide has shown enhanced electrochemical performance due to the synergistic and configurational entropy effects [35, 40].

In our earlier work, 10% Ti⁴⁺-doped P2-type NMN cathode has shown significantly improved rate performance [28]. In this work, the impact of Ti (10%) and Al (varied) co-doping on the crystal structure and electrochemical behavior of P3-type Mn/Ni-based layered oxide is reported. It is important to note that the substitution of Mn⁴⁺ by a lower oxidation state Al³⁺ allows for an increase in the Na content in the crystal structure, which is expected to improve the specific capacity. The resultant compositions, $Na_{2/3+x}Mn_{0.57-x}Al_xTi_{0.10}Ni_{1/3}O_2$ with x=0, 5%, 10%, 15%, and 20% (referred to as hereinafter, NMAT-0, NMAT-10, NMAT-10, NMAT-15, and NMAT-20, respectively) exhibited monophasic P3 and P3/O3 biphasic structures with O3 phase fraction increasing with the increase in the Al3+ content. The advantage of P3 type phases is their lower synthesis temperatures, which require less energy compared to P2/O3 phase and hence, lower cost of production. Moreover, a lower synthesis temperature yields powder with smaller average particle size. This is expected to lead to better rate performance due to the shorter Na-ion diffusion path. The electrochemical properties of NMAT-x cathodes were tested in the voltage window of 2.0-4.2 V and 1.5-4.2 V to observe the effect of varied Al content on the electrochemical behavior and the various phase transformations along with the suppression of the Jahn-Teller distortion. NMAT-10 (with 10% Al) cathode exhibited the best rate performance, highest specific capacity, and better capacity retention of 99.1% and 95.5% in the voltage window of 2.0-4.2 V and 1.5-4.2 V among all samples. Operando Synchrotron XRD studies confirmed that 10% Al doping imparts excellent electrochemical properties by limiting the extent of P'3 ↔ O'3 transformation and by modifying the P3/O3 phase structure at lower voltages during the charge-discharge process.

2. EXPERIMENTAL SECTION

2.1. Synthesis

The powder samples for $Na_{2/3+x}Mn_{0.57-x}Al_xTi_{0.10}Ni_{1/3}O_2$ with x = 0, 0.05, 0.10, 0.15, and 0.20 were prepared by the conventional sol-gel method using the stoichiometric ratio of Na_2CO_3 , $C_4H_6MnO_4\cdot 4H_2O$, $C_4H_6NiO_4\cdot 4H_2O$, $Al(NO_3)_3\cdot 9H_2O$, and $C_6H_{16}O_6N_2Ti(OH)_2$ as precursors, which were dissolved in deionized water (DI). The resultant mixture was kept for stirring to get a homogeneous mixture. For gel formation, ethylene glycol and citric acid were added in a 1:2 molar ratio. The formed gel was then dried by heating it at 120 °C. Denitrification and decarbonization were done by heating the resultant powders at 650 °C for 12 h. Finally, powders were heated at 750 °C for 12 h to obtain the desired phase. The as-prepared powder samples were stored and handled in an argon-filled glovebox.

2.2. Material Characterization

Room temperature X-ray diffraction (XRD) patterns for the phase confirmation of powder samples were collected with the help of an Empyrean diffractometer from Malvern Panalytical (Cu-K $_{\alpha}$ radiation wavelength $\lambda \approx 1.54$ Å). The scan was conducted in the 2 θ range of 10° to 70°. An inductively coupled plasma optical emission spectrometer (ICP-OES; Model: Agilent 5800) was used to determine the elemental compositions of as-prepared NMAT-x samples. Scanning electron microscopy (SEM) and energy dispersive X-ray spectroscopy (EDS) analysis were performed on as-synthesized samples (using FESEM model JEOL-7610). A Tecnai G 2 20 S-TWIN transmission electron microscopy (TEM) was used for TEM studies, and samples were prepared by drop-casting the powder on the carbon-coated Cu grids.

The oxidation states of various elements in the samples were confirmed by the X-ray photoelectron spectroscopy (XPS) data (Thermofisher Scientific Naxsa instrument, Al-Kα x-ray source with 1486.6 eV). The scanning EXAFS beamline (BL-9) at the Indus-2 synchrotron source (2.5 GeV, 150 mA) at Raja Ramanna Centre for Advanced Technology (RRCAT), Indore (India) was used to record the Mn and Ni K-edge EXAFS (extended X-ray absorption fine structure spectroscopy) data. Operando synchrotron X-ray diffraction studies were carried out using extreme conditions—angle dispersive/energy dispersive synchrotron with a beam

energy of 2.5 GeV (wavelength ~ 0.7388 Å) at Indus-2 beamline 11, RRCAT, to investigate phase transformations in pure P3 and P3/O3 biphasic samples during a charge-discharge cycle at constant current.

2.3. Electrochemical measurements

The electrochemical studies of the cells were carried out on CR2032 coin cells, which use Na metal as the anode, Whatman GF/D as the separator, and a mixture of 1M NaClO₄ in a 1:1 volumetric ratio of ethylene carbonate and propylene carbonate (EC: PC). Positive electrodes were prepared by mixing 75 wt.% active material, 10 wt.% Ketjenblack, and 15 wt.% PVDF (polyvinylidene Fluoride) in NMP (solvent). The prepared slurry was then coated on an Al current collector and dried at 120 °C for 8 h in a vacuum oven. Once dried, the cathodes were punched into 14 mm diameter discs. Na-metal and hard carbon were used as anodes for half and full cells.

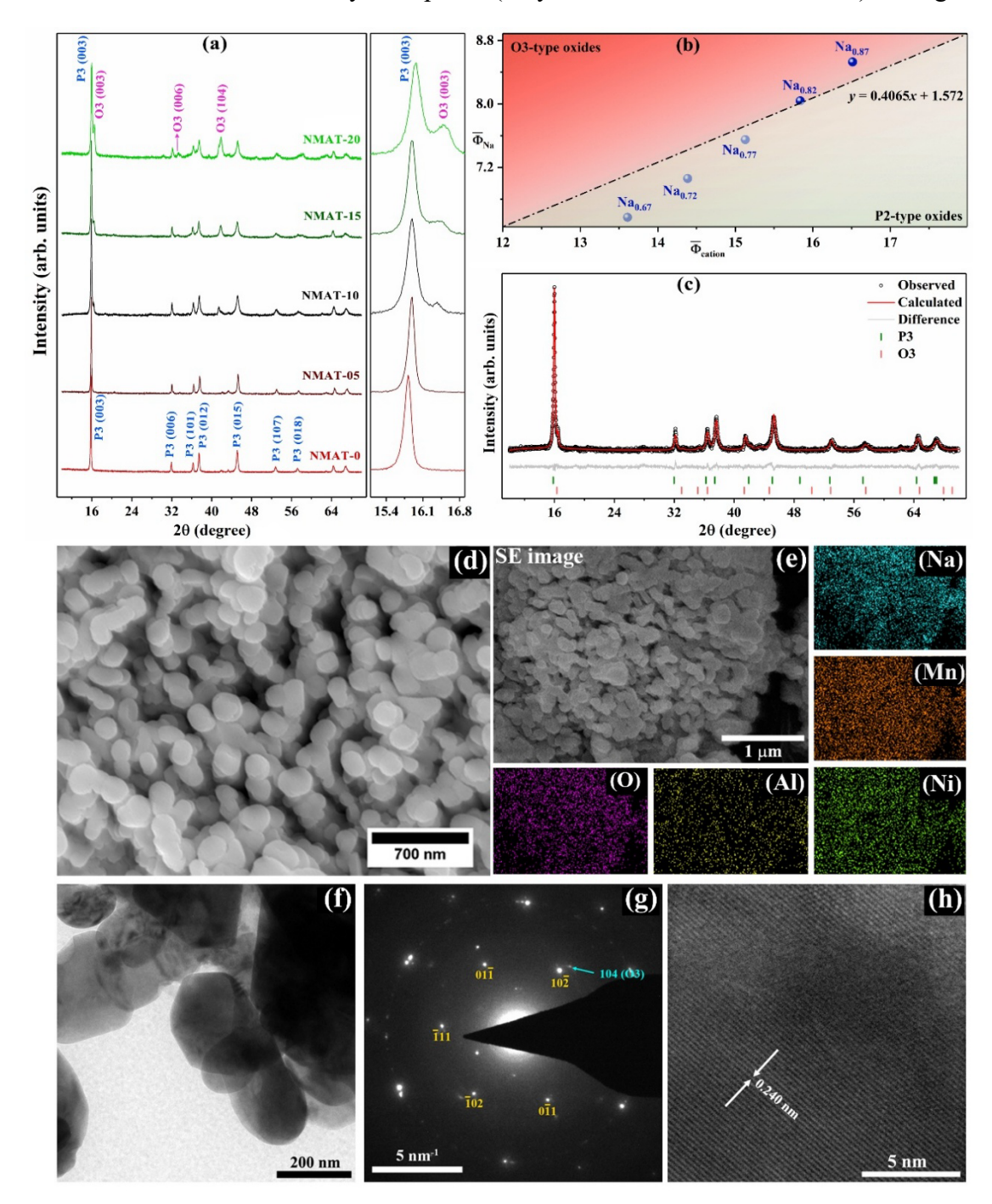
For the hard-carbon half-cell, a Swagelok-type cell was used with HC coated on an aluminum foil as the working electrode and Na metal as the anode. Electrochemical measurements like cyclic voltammetry (CV) and electrochemical impedance spectroscopy (EIS) were collected on a coin cell in the voltage range of 1.5-4.2 V with a scan rate of 0.1 mV/s using a Biologic SP-150e instrument. The galvanostatic intermittent titration technique (GITT) at 0.1C and galvanostatic charge-discharge (GCD) behaviors at various C-rates (1C = 130 mA g⁻¹) were studied using Neware battery testers, model CT-4008. The specific capacity, rate performance, and cyclability were compared for all samples in two different voltage windows, from 1.5 to 4.2 V and from 2.0 to 4.2 V.

3. RESULTS AND DISCUSSIONS

3.1. Structural characterization

Room temperature XRD was carried out to confirm the phase structure of the NMAT-x (x = 0, 05, 10, 15, and 20) samples calcined at 750 °C via the sol-gel method. Fig. 1(a) shows the XRD patterns of all five samples. Preliminary analysis of the XRD pattern of the NMAT-0 sample showed the formation of the P3 phase (space group R3m). Minor impurity peaks corresponding to the NiO phase (space group $Fm\bar{3}m$) were also observed at ~ 37° and 43°. For other samples also, all major peaks matched those of the P3 phase [41]. In addition, the peaks corresponding to the O3 phase (space group $R\bar{3}m$) are also observed in the NMAT-10 sample, confirming the biphasic nature of this sample. With a further increase in sodium content, the relative intensities

of the peaks of the O3 phase increase, suggesting an increase in the O3 phase fraction. In addition to P3, O3, and minority NiO peaks (only in NMAT-0 and NMAT-05), no significant



spurious peaks were observed, suggesting the uniform incorporation of the Al³⁺ into the lattice.

Fig. 1: (a) XRD patterns of NMAT-*x* (*x* = 0, 5, 10, 15, and 20) samples, (b) cationic potential plot for NMAT-*x* samples with different Na content, and (c) representative Rietveld refinement of XRD pattern of P3/O3 biphasic NMAT-10. (d) SEM image of the NMAT-10 sample. (e) A secondary electron (SE) image of the NMAT-10 sample and EDS elemental mappings. (f) Bright-field TEM image, (g) SAED pattern, and (h) high-resolution TEM image showing lattice fringes corresponding to (012) planes of P3 phases of the as-prepared NMAT-10 sample.

The crystal structure of the P3 and O3 (shown in Fig. S1, Supplementary material) phases can be differentiated based on the ratio of TM-O2 and Na-O2 interlayer spacing, which primarily depends on the electronic distribution in their structure. The *cationic potential*, given by equation 1, is considered a simple descriptor for the prediction of phase type (P or O), considering the sodium and transition metal contents in the composition.

$$\overline{\Phi}_{cation} = \frac{\overline{\Phi}_{TM}\overline{\Phi}_{Na}}{\overline{\Phi}_{O}} \tag{1}$$

Here, $\overline{\Phi}_{TM}$ and $\overline{\Phi}_{Na}$ denote the weighted average ionic potential of TMs and Na, respectively. $\overline{\Phi}_0$ is the ionic potential of oxygen [42]. The ionic potential is given by the ratio of the charge number and the ionic radius, reflecting the polar strength of a given cation. The Na potential versus average cationic potential plot for the NMAT-x (Na_{0.67}, Na_{0.72}, Na_{0.77}, Na_{0.82}, and Na_{0.87}) samples is shown in Fig. 1(b). The figure suggests that with the increase in sodium content from 0.67 to 0.87, the predicted phase changes from a P2-type to an O3-type. The XRD results broadly agree with the predicted trend. The phase map indicates that a small change in the Na/Al content from 5% to 10% in these samples led to the transition from a single P3 phase (for NMAT-05) to P3/O3 biphasic NMAT-15. The further increase in the intensity of O3 phase peaks for NMAT-20 can be rationalized by increased Na content (Na_{0.87}), which stabilizes the O3 phase as a consequence of shielding the electrostatic repulsion of the TM-O2 slabs. On the other hand, the stronger electronic cloud of TM, along with less sodium content, increases the electrostatic repulsion of the Na-O2 layers, resulting in a P3 structure. It is important to note that pure P3 phase was not achieved in any of the samples with x > 0.05. Similarly, higher calcination temperature led to conversion of the P3 phase to P2-type phase, and pure O3 phase was not achieved in any of these samples.

For the quantification of the different phases, Rietveld refinement of XRD data using TOPAS 6.0 academic software was carried out, and the representative fitted profile for the sample with 10% Al content (NMAT-10) is shown in Fig. 1(c) [43]. The Rietveld fitted profiles for other samples (NMAT-0, NMAT-05, NMAT-15, NMAT-20) are shown in Fig. S2(a-d). The values of the calculated lattice parameters and other crystallographic parameters for all five samples are shown in Tables 1 and S1 (Supplementary material). The low values of fitness parameters (R_{exp} , R_{wp} , R_p , and GOF) for all samples confirm a good match between the experimental data and calculated profiles. With the increase in the Na and Al content in the NMAT samples, the fraction of the O3 phase increased from ~12% for NMAT-10 to ~37% for NMAT-20. This increase in the O3 phase fraction can be attributed to the increased shielding effect between the TM-O2 slabs. Due to the balancing of the shielding effect of Na⁺ and the strong interlayer electrostatic repulsion caused by the presence of the TMⁿ⁺ layer, the NMAT-10, NMAT-15, and NMAT-20 have a P3/O3 biphasic structure.

As seen from Table 1, the c lattice parameter decreases with the increase in Al content for both P3 and O3 phases. This decrease in c is due to the stronger Al-O (512 kJ mol⁻¹) bond as compared to the Mn-O bond (394 kJ mol⁻¹) [44, 45]. Furthermore, increased Na-ions in the Na-O2 layer decrease the O^{2-} O^{2-} repulsion, which consequently reduces the lattice parameter c.

Interestingly, the decrease in the value of c is much smaller for the P3 phase (from 16.803 Å for NMAT-0 to 16.761 Å for NMAT-20) as compared to that of the O3 phase, for which c decreases from 16.291 Å for NMAT-10 to 16.227 Å for NMAT-20. This difference in the variation of c may suggest the different Na contents in the O3 and P3 phases. The values of lattice parameter a show only marginal changes with the increase in Na/A1 content, and no clear trend is observed in either of the phases. The amounts of sodium, manganese, nickel, aluminum, and titanium in NMAT-x samples were confirmed using the inductively coupled plasma optical emission spectrometer (ICP-OES), and the results are provided in Table S2. The calculated amounts of various elements match well with the samples' nominal compositions.

Table 1: The lattice parameters (a and c) and phase fractions (PF) of P3 and O3 in NMAT-x samples.

		NMAT-0	NMAT-05	NMAT-10	NMAT-15	NMAT-20
	a (Å)	2.8944(1)	2.8997(6)	2.8929(1)	2.9003(1)	2.8981(2)
Р3	c (Å)	16.803(2)	16.795(1)	16.786(2)	16.770(1)	16.761(3)
	PF (%)	98 (2% NiO)	99 (1% NiO)	88	75	63
	a (Å)	-	-	2.9840(4)	2.9509(3)	2.9587(43)
03	c (Å)	-	-	16.291(3)	16.258(3)	16.227(3)
	PF (%)	0	0	12	25	37

The representative SEM image in Fig. 1(d) shows the morphology of the NMAT-10 powder sample. The average size of the spheroid particles is ~200 nm, with a large distribution in sizes. For other samples, SEM images (Fig. S3) show highly agglomerated particles of similar morphologies. With the increase in Na/Al content in NMAT samples, the particles seem to be more agglomerated; however, no significant change in average size is discernible. EDS elemental mappings for the NMAT-10 sample confirm the uniform distribution of constituent elements throughout the sample, as shown in Fig. 1(e1-e5). The SEM and XRD analyses confirm the incorporation of Na/Al in the NMAT crystal structure.

The crystal structure of the NMAT-10 sample was further examined using transmission electron microscopy (TEM). The recorded bright field image, selected area diffraction (SAED) pattern, and high-resolution (HRTEM) are shown in Figs. 1(f), 1(g), and 1(h), respectively. Agglomeration of particles is observed in Fig. 1(f). The main diffraction spots in Fig. 1(g) belong to the P3 crystallite oriented with its [121] direction parallel to the electron beam. These

spots correspond to the $(10\overline{2})$, $(01\overline{1})$, $(\overline{1}11)$, $(\overline{1}02)$, and $(0\overline{1}1)$ planes of the NMAT-10 sample (R3m phase). Additional diffraction spots, observed in Fig. 1(g), belong to the O3 phase (indicated by the arrow) and other agglomerated P3 crystallites. The regular lattice fringes observed in the HRTEM image (Fig. 1(h)) confirm the crystallinity of the sample. The lattice fringe spacing of 0.240 nm corresponds to the (102) crystal plane of the P3 phase of the NMAT-10 sample.

X-ray photoelectron spectroscopy was performed on the NMAT-x samples to analyze the oxidation states of the various constituent elements. Fig. 2(a) and 2(b) show the XPS spectra for Mn 2p and Ni 2p, respectively. A survey scan for the NMAT-10 sample is provided in Fig. S4. Ni 2p spectra for all samples are fitted with two major and two additional satellite peaks. Ni 2p spectrum for NMAT-0 exhibits two distinct characteristic peaks at ~ 854.8 eV and 871.6 eV, corresponding to $2p_{3/2}$ and $2p_{1/2}$. [46]. The position of Ni 2p peaks with a spin-orbit split of ~17 eV confirms the 2+ oxidation state of Ni in NMAT-0. Broader satellite peaks are observed at ~ 860.5 eV and 879.5 eV. As the Ni 2p peaks' position did not alter noticeably on increasing x from 0 to 20, additional Na and Al content in NMAT does not seem to affect the oxidation state of Ni. Two characteristic peaks corresponding to Mn 2p spectra located at the binding energies of ~642.7 and 653.8 eV, attributed to Mn $2p_{3/2}$ and Mn $2p_{1/2}$, confirmed the presence of Mn in an oxidation state of 4+ [46]. The binding energies of Mn 2p are similar for all NMAT-x samples, confirming the presence of Mn⁴⁺ in all five samples. The binding energies for the Ti 2p were observed at ~457.5 and ~463.5 eV, corresponding to Ti $2p_{3/2}$ and Ti $2p_{1/2}$, confirming the presence of Ti in the +4 oxidation state in all samples shown in Fig. S5 [47].

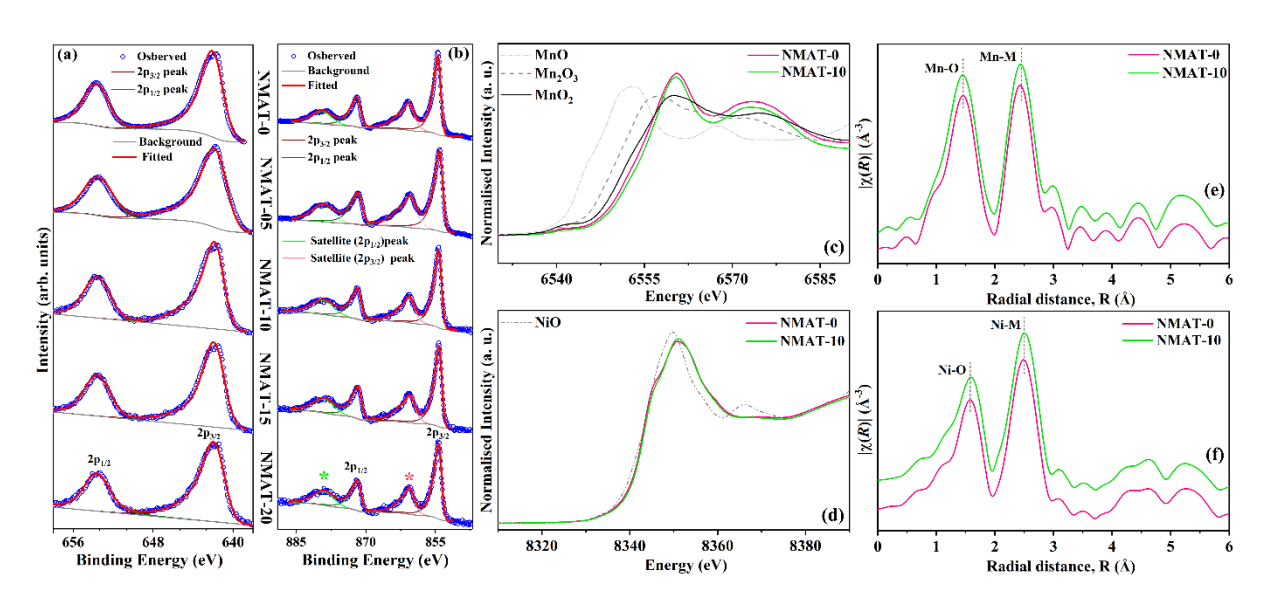


Fig. 2: (a) Experimental and fitted XPS data for Mn 2p and (b) Ni 2p for NMAT samples. XANES spectra of the pristine NMAT-0 and NMAT-10 cathodes at the (c) Mn K-edge and (d) Ni K-edge. EXAFS spectra of (e) Mn K-edge and (f) Ni K-edge.

The oxidation states and local structures of the NMAT samples were further confirmed using X-ray absorption spectroscopy. The normalized x-ray absorption near-edge structure (XANES) spectra at Mn and Ni K-edges for the NMAT-0 and NMAT-10 cathodes are shown in Figs. 2(c) and 2(d), and the corresponding extended x-ray absorption fine-structure (EXAFS) plots are given in Figs. 2(e) and 2(f), respectively. A close match of the absorption edge energies of Mn and Ni K-edges with standard MnO₂ and NiO indicates that the valencies of Mn and Ni atoms in both NMAT-0 and NMAT-10 samples are +4 (for Mn) and +2 (for Ni). The slight variations in the Mn and Ni K-edge energies of NMAT-x and standard MnO₂ & NiO are due to the difference in crystal structures. The EXAFS spectra at the Mn K-edge (Fig. 2(e) reveal scattering peaks resulting from Mn–O interaction (at ~1.46 Å) and Mn–M (M: next-nearest metal ions) interactions (at ~2.43 Å) for both samples. Similarly, in Ni K-edge spectra (Fig. 2(f)), the Ni–O (at ~1.6 Å) and Ni–M (at ~2.51 Å) peaks correspond to the scattering from the nearest oxygen anions and the next-nearest metal ions, respectively.

3.2 Electrochemical properties

Cyclic voltammetry (CV) was performed on half-cells in the voltage range of 1.5 to 4.2 V at a scan rate of 0.1 mV/s to observe the oxidation-reduction in NMAT-x samples. Fig. S6(a-e) shows the first two cycles of CV curves for all NMAT-x samples. The two prominent features in the 3.0-4.2 V voltage range in Fig. S6(a) correspond to Ni^{2+/3+} redox in NMAT-0 [48]. These oxidation peaks at \sim 3.50 V and \sim 3.85 V are reversible with a polarization of \sim 0.49 V and \sim 0.40 V for NMAT-0. For the NMAT-10 sample, these peaks shifted to lower voltages, ~3.67 V and ~3.32 V, suggesting the activation of Ni at a lower potential in Al-substituted samples. The polarization in corresponding redox peaks decreased to 0.19 V and 0.12 V for the NMAT-10 sample. For the NMAT-20, the same trend of voltage shift to lower voltage can be observed. It can be due to the increase in the phase fraction of the O3 phase. As a result of increased Na content in the O3 phase, it is easier to remove the Na from the cathode, which lowers the redox voltage. In addition to the voltage shift, one incomplete peak in the NMAT-10 sample can be observed in the NMAT-20 sample, which is not completely reversible. The shift in the redox voltage can be due to the different energy required for desodiation-sodiation in NMAT-x samples with varied Na contents, even with the same amount of Ni. The redox peak at a lower voltage (below 2.5 V) is due to the $Mn^{3+/4+}$ activation [17, 49].

To evaluate the electrochemical performance of NMAT-x cathodes, galvanostatic chargedischarge (GCD) measurements were done on CR2032 cells (in half-cell configuration) in two different voltage ranges, 1.5-4.2 V and 2.0-4.2 V. The upper cut-off voltage was limited to 4.2 V as charging above this voltage led to a capacity loss, possibly due to the irreversible anionic redox and/or electrolyte decomposition [50]. The choice of two different low cut-off voltages was to ascertain the impact of increased Na⁺ content and Al³⁺ substitution for Mn³⁺ on the cyclability and Jahn-Teller active Mn^{3+/4+} redox. Fig. 3(a-b) depicts the first charge-discharge and differential capacity (dQ/dV) vs. voltage (V) curves of all five (NMAT-x) samples in 2.0-4.2 V, respectively. The first charge-discharge cycle for all the NMAT-x cells was carried out at 0.1 C. In the 2.0-4.2 V range, the initial discharged specific capacity for the NMAT-0 sample was ~91 mAh g-1. With the increase in Al content from 0 to 20%, the capacity first increased from ~91 mAh g⁻¹ for NMAT-0 to ~100 mAh g⁻¹ for NMAT-10 and then gradually decreased to ~82 mAh g⁻¹ for NMAT-20. A similar trend was observed in the specific capacities in the voltage window of 1.5-4.2 V, shown in Fig. 3(c), where the initial specific capacity decreased from ~166.6 mAh g⁻¹ for NMAT-0 to ~117.2 mAh g⁻¹ for NMAT-20. Again, the NMAT-10 sample showed the highest discharge capacity of ~175.5 mAh g⁻¹. Surprisingly, the NMAT-05 and NMAT-15 samples showed a discharge capacity of only ~164.5 mAh g⁻¹ and ~137.7 mAh g⁻¹, respectively.

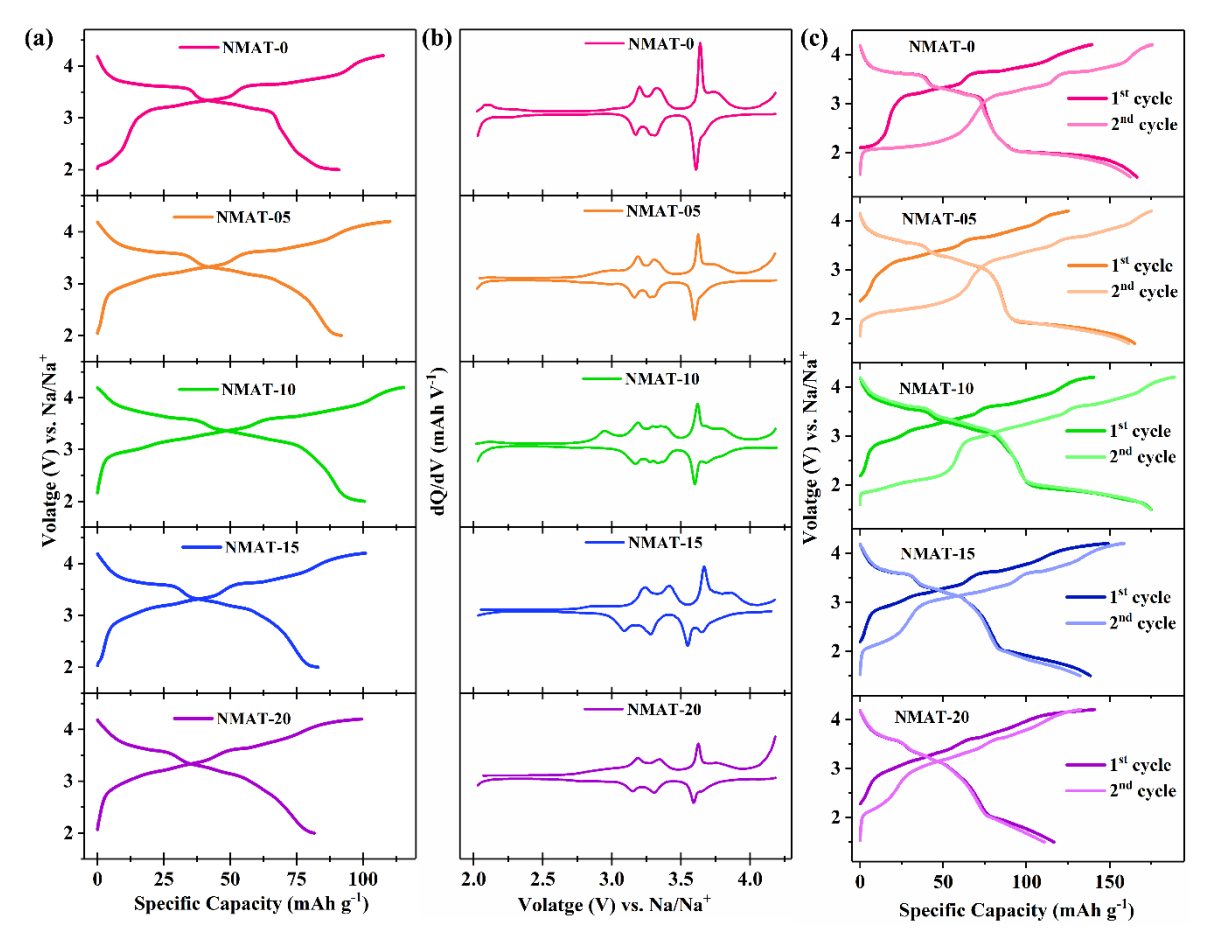


Fig. 3: (a) First GCD cycle and (b) the dQ/dV vs. V plots for NMAT samples at 0.1C in the 2.0-4.2 V range. (c) First two GCD cycles of NMAT samples at 0.1 C in the 1.5-4.2 V range.

The increase in the initial discharge capacity can be attributed to the introduction of additional Na-ions in the NMAT-10 sample (0.77 Na vs. 0.67 Na in NMAT-0). In the 2.5 – 4.2 V range, the Ni^{2+/3+} redox couple is primarily responsible for the charge compensation [7, 48, 49]. Multiple voltage plateaus in the charge-discharge profile of NMAT-*x* are observed in Fig. 3(a). These plateaus correspond to the various phase transformations, including Na-ion/vacancy ordering and transition metal ordering, during the cathode's charging and discharging [27, 51]. Another impact of increased Al³⁺ in TM layers (which is concomitant with increased Na content and O3 phase fraction) is the smoothening of plateaus in GCD curves, which is evident from the broadening of peaks in the differential capacity (dQ/dV) vs. voltage (V) plots (Fig. 3(b)). Such solid-solution type insertion/extraction behavior has been reported in other *pillar*ions doped layered oxides [31, 51-55]. While such cathodes show better cyclability due to the suppressed phase transitions, this is usually accompanied by a decreased specific capacity at low C rates [56]. The decrease in the initial specific capacity for NMAT-15 and NMAT-20 cathodes could be attributed to the smoothening of the Ni-redox (Ni^{2+/3+}) plateau with

increasing Na/Al content [51]. The voltage plateaus observed in the charge-discharge profiles are consistent with the CV and the dQ/dV vs. V plots. An additional plateau below 2.0 V during discharging (Fig. 3(c)) is attributed to the Mn⁴⁺ to Mn³⁺ reduction [15].

It is to be noted that for the NMAT-20 sample, the amount of Na at OCV is 0.87, which implies that only \sim 0.13 Mn⁴⁺ can be reduced to Mn³⁺ during the first discharge. This corresponds to a capacity of \sim 30 mAh g⁻¹ due to Mn redox. Accordingly, the overall specific capacity is lower in 1.5-4.2 V range for samples with higher Na/Al contents. Further, with the increase in Na/Al content, the discharge plateaus shift to lower voltages, which is also reflected in the shifting of peaks in dQ/dV vs. V curves to lower voltages. This could be due to the increased O3 content in Al-doped samples. O3 phases with higher Na content are reported to have a lower average potential for Ni^{2+/3+} than their P-type counterparts [28, 57-59].

Fig. 4(a & b) shows the rate performance of NMAT-0, NMAT-10, and NMAT-20 samples at various discharge currents corresponding to 0.1C, 0.2C, 0.3C, 0.5C, 1C, 2C, 3C, and 5C in 2.0-4.2 V and 1.5-4.2 V windows, respectively. The corresponding rate performance for NMAT-05 and NMAT-15 samples is shown in Fig. S7. For all the samples, the discharge capacity decreased with an increased C-rate in both voltage ranges. The decrease in the discharge capacity values was lower for the NMAT-10 sample than for the rest of the NMAT-x samples. In the 2.0-4.2 V range, the discharge capacity decreases from 101 mAh g⁻¹ at 0.1C to 81 mAh g⁻¹ at 5C for the NMAT-10 cathode. The discharge capacities for NMAT-0, NMAT-05, NMAT-15, and NMAT-20 at 5C were 60%, 74%, 77%, and 63%, respectively, of their corresponding capacity at 0.1C, as shown in Fig. 4a. Similarly, in the voltage range of 1.5-4.2 V, the discharge capacities at 5C were 35.5%, 43.4%,53%, 42.7%, and 33.3% for NMAT-0, NMAT-05, NMAT-10, NMAT-15, and NMAT-20, respectively, of the initial capacity at 0.1C. In both voltage ranges, the NMAT-10 sample showed a better discharge capacity even at a high C-rate. This shows that 10% Al helps stabilize the cathode and suppresses the sudden phase transformation. The polarization values also corroborate the same. The substantial variation in the rate performances in Na/Al-doped could be due to the increased O3 phase fraction.

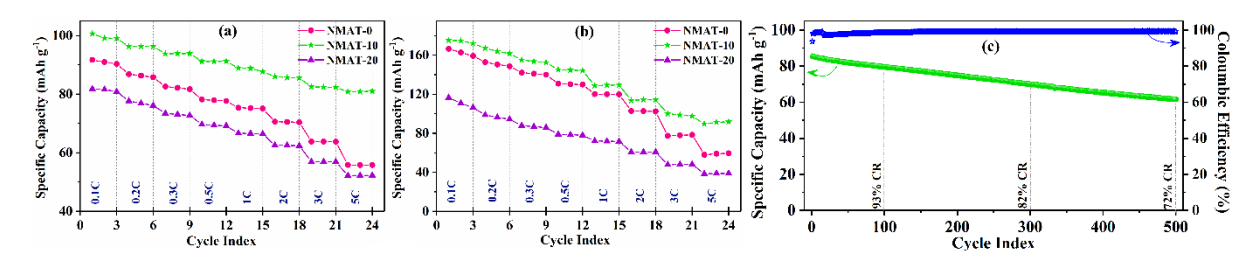


Fig. 4: Rate performance of NMAT-0, NMAT-10, and NMAT-20 samples in the voltage range of (a) 2.0-4.2 V and (b) 1.5-4.2 V. (c) Cycling performance of NMAT-10 at 2C.

The O3 phases are known to have a smaller bottleneck area for the Na-ion migration as compared to P-type phases, leading to poor rate capabilities in NMAT-15 and NMAT-20 cathodes [11, 60]. In the P3 type structure, the bottleneck for Na-ion diffusion is rectangular, which has a significantly larger area than the triangular bottleneck for O3-phases. Therefore, the sample with a higher P3 phase is expected to have a superior rate performance [61]. In the O3-type structure, the smaller triangular bottleneck area for Na-ion diffusion is responsible for poor Na-ion diffusion [62]. Additionally, with the increase in Na/Al content, the particles seem to be more agglomerated. The grain boundaries in agglomeration tend to impede the Na-ion diffusion. It is important to note that during the charge-discharge process, P3 and O3 phases undergo several transformations. Formation of resulting phase boundaries is detrimental for facile Na-ion conduction, and it becomes the rate-determining factor. Suppression of these phase transformations improves not only the cyclability but also the rate performance of these cathodes. As demonstrated by the operando SXRD data (discussed later), the constrained P3↔P3'↔O3 phase transformations in NMAT-10 result in a better rate performance than NMAT-0, despite having a 12% O3 phase.

The results of cycling stability of the NMAT-*x* cathode materials tested at 0.3C in the 2.0 to 4.2 V and 1.5 to 4.2 V voltage ranges are displayed in Fig. 5 and Fig. S9, respectively. In 2.0-4.2 V, after 50 cycles, the capacity retention of NMAT-0, NMAT-05, NMAT-10, NMAT-15, and NMAT-20 is ~91%, 95.8%, 99%, 94.7%, and 88.3%, respectively (Fig. 5(f)). A similar trend in capacity retention is observed in the voltage range of 1.5-4.2V, as shown in Fig. S9(f). In both voltage windows, the NMAT-10 cathode shows better cyclability. Therefore, it is inferred that the cathode with the majority P3 and minority O3 phase shows better cyclability than the pure P3 phase. Among the five NMAT-*x* samples, NMAT-10 showed the best overall electrochemical performance, starting from the higher initial discharge capacity at 0.1C to better rate performance and cyclability. Typically, the cyclability of layered oxide is governed by the phase transitions during the GCD process. The nature of phase changes in NMAT-0 and

NMAT-10 during the charge-discharge process is discussed in the operando SXRD section. The long-term cyclability at a high C-rate (2C) is also performed on the NMAT-10 sample, and the result for the 2.0-4.2 V range is shown in Fig. 4(c). The cyclability for the NMAT-0 and NMAT-20 samples at 2C is provided in Fig. S10. Among all samples, NMAT-10 shows the best cyclability with capacity retention of ~82% after 300 cycles and ~72% after 500 cycles. The corresponding capacity retentions for the NMAT-0 and NMAT-20 are ~79% and ~73% (after 300 cycles) and ~68% and ~60% (after 500 cycles), respectively. These results confirm that 10% Al doping not only improved the rate performance and the initial discharge capacity but also helped in better cyclability.

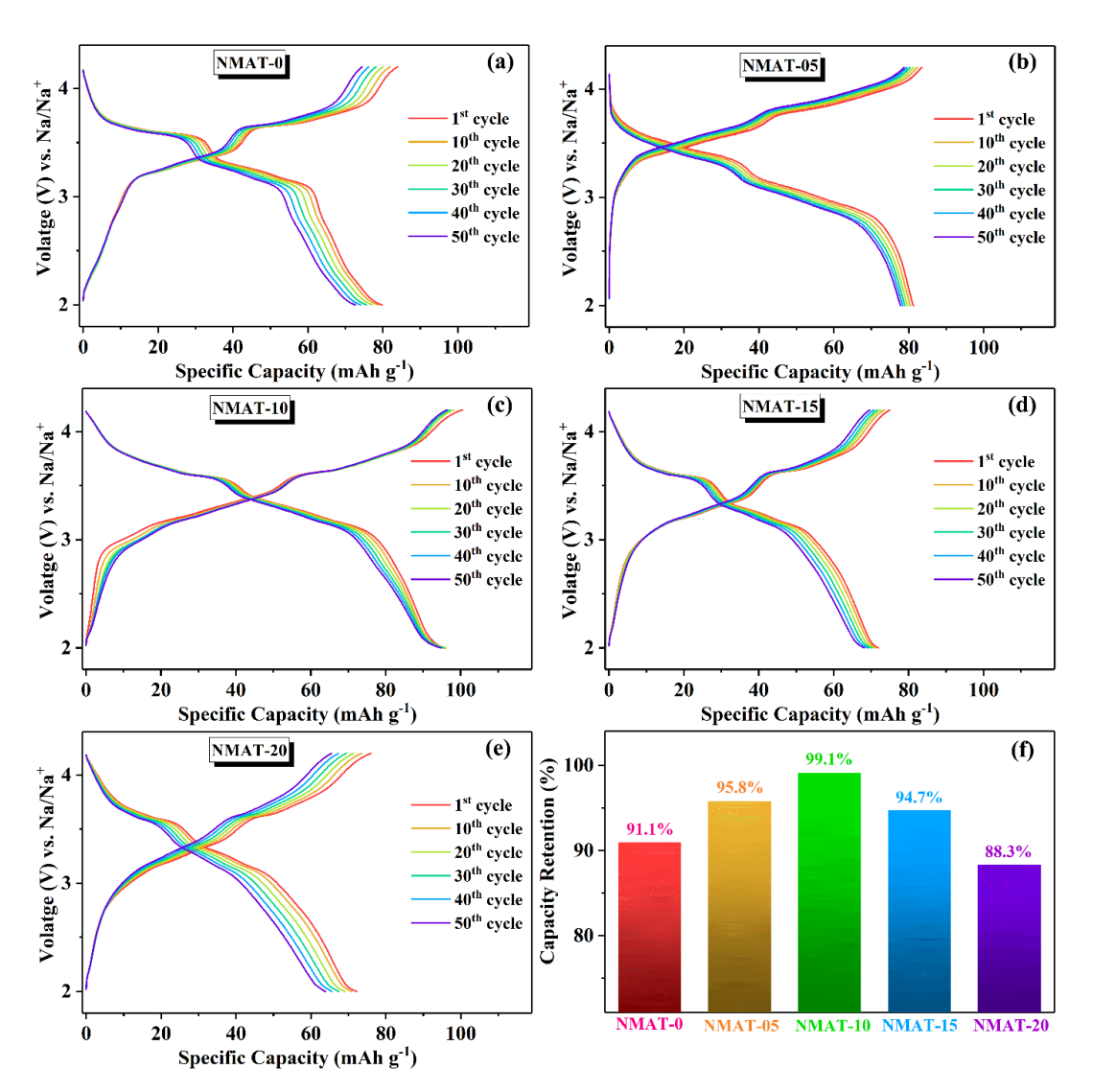


Fig. 5: Cyclic performance of NMAT-x samples in the 2.0-4.2 V voltage window, along with the capacity retention plot (f).

A comprehensive charge-discharge analysis for the Na^+ ion diffusion utilizing GITT was performed for all NMAT-x samples. The obtained GITT plots (voltage, V vs. time, t), along

with the diffusion coefficients for NMAT-0 and NMAT-10 samples, are shown in Fig. 6(a-b). Na-ion diffusion coefficients were calculated using equation (2),

$$D_{Na^{+}} = \frac{4}{\pi \tau} \left(\frac{m_B}{\rho S}\right)^2 \left(\frac{\Delta E_S}{\Delta E_{\tau}}\right)^2 \tag{2}$$

Where D_{Na}^+ represents the sodium ion diffusion coefficient, and ΔE_{τ} & ΔE_{S} are the voltage changes during the current pulse & when the cathode reaches equilibrium. S, ρ , m_{B} , and τ are the cathode's surface area, the cathode material's molar density, active material loading, and the duration of the constant current pulse, respectively.

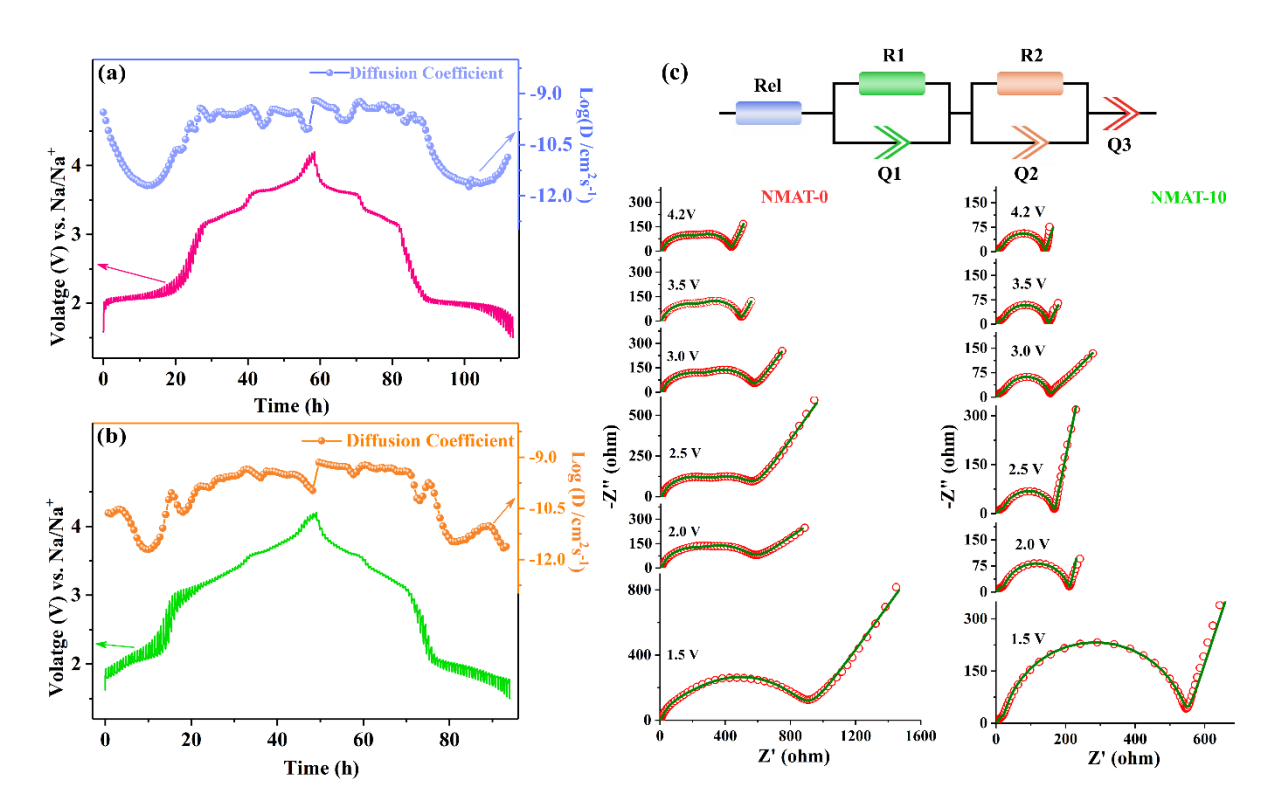


Fig. 6: GITT curves of (a) NMAT-0 and (b) NMAT-10 samples along with the diffusion coefficient. (c) Room temperature Nyquist plots of NMAT-0 and NMAT-10 samples, along with the equivalent circuit used for fitting impedance data.

From the values of diffusion coefficients for different samples, it is observed that the D_{Na}^+ is highest for the NMAT-10 ($7 \times 10^{-10} - 2 \times 10^{-12}$ cm² s⁻¹) and lowest for the NMAT-20 ($2 \times 10^{-10} - 4.5 \times 10^{-14}$ cm² s⁻¹). The variation in the Na-ion diffusion coefficients in cathodes at different stages during charging-discharging is attributed to two factors. Firstly, the kinetics of Mn^{3+/4+} and Ni^{2+/3+} redox processes [55]. At cell voltage below 2.5 V, the charge compensation mechanism is Jahn-Teller active Mn^{3+/4+} redox, which seems to be the rate-limiting step.

Secondly, sodium deintercalation from the crystal structure increases the number of Na-ion vacancies in the Na layers, facilitating Na-ion hopping. Further, removal of the Na-ion also increases the Na-O2 layers spacing and leads to improved Na⁺ diffusion. However, at higher charging voltages, further desodiation of these samples causes structural transformation to O-type phases. These phases may impede the diffusion due to the triangular bottlenecks in octahedrally coordinated Na-ions. These competing mechanisms are responsible for the observed variations in D_{Na}^+ during the charge-discharge process. Overall lower values of D_{Na}^+ for NMAT-20 samples could be due to increased particle agglomeration in this sample, as well as the nature of phase transformations during cycling. It is to be noted that the O3 phases are known to have sluggish Na⁺ migration. Accordingly, the monophasic P3 sample (NMAT-0) is expected to have higher D_{Na}^+ . However, as discussed later in the operando x-ray diffraction section, the NMAT-0 exhibited a significant O3 phase fraction when discharged to 1.5 V. The slower diffusion of Na-ion is responsible for the poor rate performance of the NMAT-20 sample. The GCD and GITT results confirm that Al content > 10% is not suitable for further improving the electrochemical performance of NMAT-x cathodes.

The electrochemical impedance spectroscopy was used to probe the mechanism for the better performance of the NMAT-10 cathode. These measurements were done at room temperature in the frequency range of 100 kHz to 10 mHz by applying a 10 mV signal. The Nyquist plots for the NMAT-0 and NMAT-10 cells are shown in Fig. 6(c) at different states of charge (SOCs). Nyquist plots show two overlapping semicircular arcs in the high-frequency region along with a tail in the lower-frequency region. An equivalent circuit (Fig. 6(c) inset) fitting was used to estimate the various contributions to the overall impedance of the cell. The values of various components' resistances plotted against cell voltage are shown in Fig. S11(a) (for NMAT-0) and S11(b) (for NMAT-10). The NMAT-10 cell showed a much lower resistance than the NMAT-0 cell at all voltages. Electrolyte resistance (Rel) does not vary with the state of charge for either cell. With the increase in the cell voltage, overall cell resistance (R_{total}) decreases for both cells, with charge-transfer resistance (R2) contributing predominantly to this decrement. The values of R1 (which represents the interfacial layers' resistance) are significantly lower for the NMAT-10 sample than those of NMAT-0 at all cell voltages. Further, the interfacial resistance shows only minor changes with increasing cell voltage for the NMAT-10 cell. This suggests better interfacial layer stabilization in the NMAT-10 sample. The charge transfer resistance for both samples decreases monotonically with an increase in cell voltage. For the NMAT-0 cell, R2 decreases from $661\pm2~\Omega$ at 1.5 V to $204\pm2~\Omega$ at 4.2 V; the corresponding change for the NMAT-10 cell is from $520\pm2~\Omega$ to $130\pm1~\Omega$. A significant decrease in the charge transfer resistance, on increasing the cell voltage to $\sim2.0~V$, is due to the onset of the Mn^{3+/4+} redox reaction. Further decrease in R2 at 3.0 V is due to the stabilization of the Ni^{2+/3+} redox reaction.

At 4.2 V and 1.5 V, the overall resistance of the NMAT-10 is ~149 Ω and ~545 Ω , respectively. While for the NMAT-0 sample, the corresponding values are ~429 Ω and ~885 Ω . As a result of lower cell resistance and lower charge–transfer and interfacial layer resistance, the rate and cyclic performance are better in the NMAT-10 sample than in the pristine NMAT-0. Hence, 10% Al doping helps achieve better electrochemical performance of the NMAT- α cathodes.

3.3. Operando Synchrotron XRD

An in-depth investigation of the NMAT-0 and NMAT-10 cathodes was carried out using operando synchrotron XRD in half-cell configurations to further evaluate the impact of Al substitution on the structural evolution during the charge-discharge process. These measurements were conducted in the voltage range of 1.5 V to 4.2 V with a current density of 26 mA g⁻¹ using CR2032 coin cells with 3 mm diameter holes sealed with Kapton film. The SXRD results for NMAT-0 and NMAT-10 samples are shown in Fig. 7(a) and 7(b), respectively. The color contour plots for selected peaks are shown in Fig. S12 and S13. During Na-ion extraction from the NMAT-0 cathode, (003) and (006) peaks of the P3 phase shift toward the lower angles, signifying an increase in the lattice parameter c. This increase in c is due to the increased O²⁻– O²⁻ repulsion as a consequence of reduced Na content in the Na-O2 layer. On the other hand, P3(101) and P3(102) peaks shift towards higher angles as expected. Upon charging above 3.1 V, the P3(105) peak broadens and shifts towards a higher angle, which is indicative of the transformation of the P3 phase into a monoclinic P'3 phase [63]. The intensity of P3(101), P3(102), and P3(105) peaks decreases drastically and flattens out when the cell is charged to 4.2 V (Fig. S12). These results confirm that the removal of ~0.36 Na from pristine NMAT-0 converts the P3 to a desodiated-O3 type (O'3) phase via the intermediate P'3.

On discharging the NMAT-0 cathode to 2.5 V, the desodiated O'3 phase transforms back to the P'3 phase, and all peaks gradually return to their original positions, indicating a reversible phase transition to a pure P3 phase. However, further discharging to 1.5 V inserts additional Na-ions in NMAT-0, with Na content estimated to be \sim 0.90 (Na content is \sim 0.67 in the pristine sample). The charge compensation in the lower voltage plateau (below 2.0 V) is through the reduction

of Mn⁴⁺ to Jahn-Teller active Mn³⁺, as discussed earlier. The increased Na⁺ screening in Na layers leads to a decrease in the c parameter, and, as a result, there is a partial transformation of the P3 phase to the hexagonal O3 phase. This is confirmed by the appearance of (003) and (006) peaks of the O3 phase in the operando XRD patterns of the sample in high sodiated states (Fig. 7(a)).

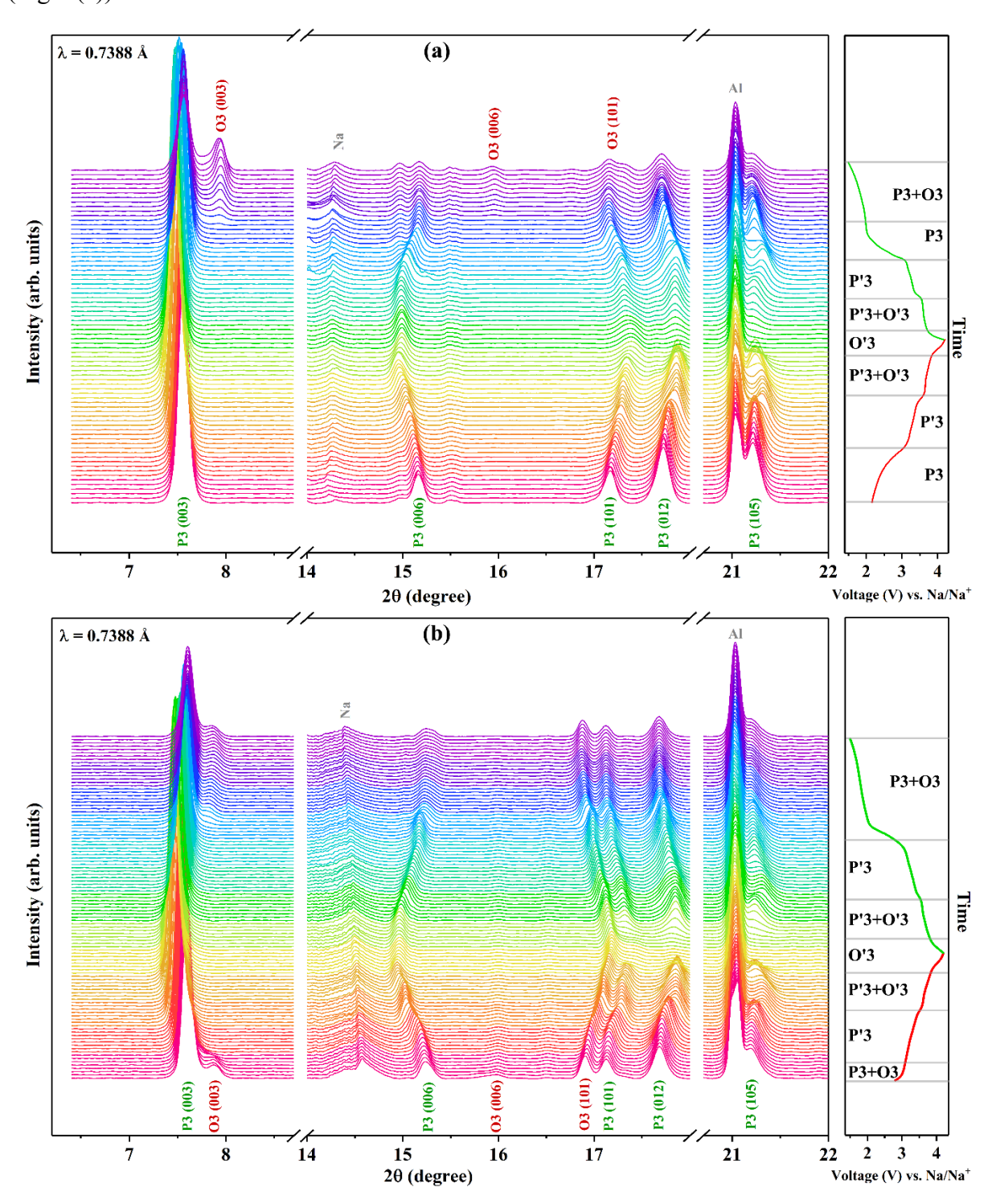


Fig. 7: Operando synchrotron XRD patterns for (a) NMAT-0 and (b) NMAT-10 samples.

NMAT-10 cathode shows a similar series of phase transitions during the charge-discharge process, with one noticeable difference concerning the presence of the O3 phase (space group $R\overline{3}m$) in the pristine sample (Fig. 7(b)). As in the NMAT-0, the P3 phase in NMAT-10 undergoes the P3 \leftrightarrow P'3 \leftrightarrow P'3+O'3 \leftrightarrow O'3 transitions. The intensity of the (003) & (006) peaks belonging to the O3 phase decreases, their positions shift towards lower angles, and they merge with corresponding peaks of the P3 phase during desodiation. During the discharging process, these peaks progressively reappear below 2.6 V, confirming the structural reversibility of the O3 phase in the GCD process. The impact of the Al incorporation on the structural evolution of the NMAT-0 during Na extraction/insertion seems to be in terms of limiting the extent of $P'3 \leftrightarrow O'3$ transformation and the nature of P3/O3 phase coexistence at lower voltages. The difference in the (003) peak positions of P3 and O3 phases, when discharged to 1.5 V, is much higher for NMAT-0 (~0.380°) compared to the NMAT-10 sample (~0.245°), as shown in Fig. S14. The estimated P3 & O3 phase fractions in NMAT-0 cathode discharged to 1.5 V are ~ 65% & 35%. As shown in Fig. 7, at OCV, the NMAT-0 sample has no O3 phase. Interestingly, at the end of the discharge cycle, NMAT-10 cathode has only about ~16% O3 phase as compared to the 12% O3 phase in the pristine sample. The better cycling performance of the NMAT-10 sample may result from the coexistence of the P3 and O3 structures in the asprepared material. The beneficial impact of Al doping is more pronounced when the NMAT cathode is cycled in the 1.5 to 4.2 V range, as Al³⁺ would suppress the cooperative Jahn-Teller distortion, which gets activated due to Mn^{4+/3+} redox.

3.4. Full Cell

The NMAT-10 half-cell utilized a Na metal foil as the anode that could also act as a large reservoir of Na-ions. For practical Na-ion cells, however, the anode typically does not provide any additional Na-ions. Accordingly, the NMAT-10 cathode, which showed excellent rate and cyclic stability, was used as the cathode, and hard carbon (HC) as the anode for the fabrication of a full cell. The GCD curves of a hard-carbon half-cell assembled using Na metal as the anode and 1M NaClO₄ in EC:PC (1:1 volumetric ratio) as the electrolyte for the first two cycles are shown in Fig. 8(a). The HC showed a specific sodiation capacity of ~ 440 mAh g⁻¹ in the first cycle. During desodiation, a reversible capacity of 266 mAh g⁻¹ is achieved, which suggests that a significant amount of Na⁺ gets irreversibly incorporated into HC. A comparison of 1st and 2nd cycle sodiation curves confirms the irreversibility of the voltage plateau around 0.7 V. The specific capacity during sodiation in 2nd cycle is ~300 mAh g⁻¹. The sodium storage in HC

is reported via a combination of adsorption, intercalation, and pore-filling phenomena in different voltage ranges [64]. To avoid the impact of poor initial Coulombic efficiency, the HC was cycled in the 0.01 V to 2.5 V range. The cycled HC electrode was harvested from the Swagelok-type cell in an inert atmosphere glovebox and used for the fabrication of the NMAT-10 full-cell. The mass loading of the cathode was balanced in a N/P capacity ratio of 1.

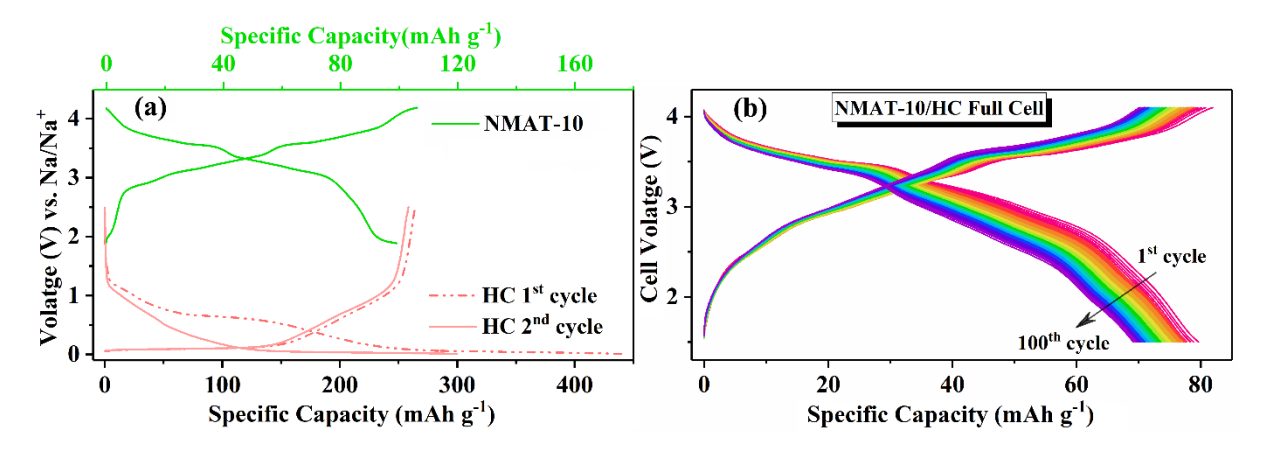


Fig. 8: (a) Formation cycle of the NMAT-10 half-cell and first two cycles for the hard-carbon half-cell at 0.1C. (b) Full cell GCD plots for the NMAT-10 cathode at 0.2C.

The full cell showed an irreversible voltage plateau when charged above 4.1 V, and the capacity faded rapidly with cycling, as shown in Fig. S15. This capacity loss, on charging to high voltages (above 4.2 V in half-cell configuration) in Mn/Ni-based layered oxides, is attributed to the irreversible anionic redox and phase transformations as reported in literature [50, 65-67]. While no such capacity fading is observed in NMAT-10 half cell (with Na metal counter electrode) charged to 4.2 V, the overall cell voltage decreases in full cell configuration due to the sodiation of hard carbon at relatively higher voltages. Accordingly, the upper cut-off voltage of the full cell was limited to 4.1 V. Fig. 8(b) shows 100 charge-discharge cycles of the full cell at 0.2C in the 1.5 - 4.1 V range. This cell showed a discharge specific capacity of ~80 mAh g⁻¹ in the first cycle, which decreased to ~69 mAh g⁻¹ after the 100th cycle. The nominal cell voltage is ~3.26 V. This remarkable capacity retention of ~86% after 100 cycles and a specific energy of ~260 Wh kg⁻¹ (considering the weight of cathode active material only) in full-cell configuration demonstrates the potential application of P3/O3 biphasic NMAT-10 in Na-ion batteries.

4. CONCLUSIONS

In summary, a series of $Na_{2/3+x}Mn_{0.57-x}Al_xTi_{0.10}Ni_{1/3}O_2$ cathode materials were synthesized via a conventional sol-gel method. By adjusting x, the O3 phase fraction in P3 phase dominant

samples was optimized, and the sample with x = 0.10 (NMAT-10) exhibited the best electrochemical performance. NMAT-10, benefiting from the P3/O3 biphasic structure, showed a reversible capacity of 101 mAh g⁻¹ in a voltage window of 2.0 to 4.2 V and 175.5 mAh g⁻¹ (1.5 to 4.2 V range) at a current density of 0.1C. This cathode showed excellent rate capability, achieving a discharge capacity of ~81 mAh g⁻¹ at a current rate of 650 mA g⁻¹. Furthermore, after 300 cycles at 260 mAh g⁻¹, capacity retention in NMAT-10 was ~83% in the 2.0-4.2 V range, confirming the superior cyclic stability. The improved rate performance in 10% Al-doped samples was attributed to a higher diffusion coefficient, as demonstrated by the GITT and EIS results. The operando synchrotron XRD analyses revealed that the P3/O3 biphasic structure of NMAT-10 suppresses the severity of the P3 \leftrightarrow P3' \leftrightarrow O3 phase transition during the charge/discharge cycle. A specific capacity of 81 mAh g⁻¹ was achieved in an NMAT-10||hard-carbon full cell at 0.2C. This study introduced a P3/O3 biphasic structure as an effective way to design layered oxide cathodes for high-performance rechargeable Na-ion batteries.

CRediT authorship contribution statement

Neha Dagar: Conceptualization, Data curation, Formal analysis, Investigation, Methodology, Validation, Writing— original draft. Samriddhi Saxena: Writing— review & editing. Velaga Srihari: Data curation, Writing— review & editing. Himanshu Kumar Poswal: Writing— review & editing. Sonia Deswal: Writing— review & editing. Pradeep Kumar: Data curation, Writing— review & editing. Sunil Kumar: Funding acquisition, Project administration, Supervision, Validation, Writing— review & editing.

Acknowledgments

This work was financially supported by the Ministry of Education (grant number: MoE-STARS/STARS-2/2023-0365). ND acknowledges the UGC-JRF scheme of the Government of India (Grant no. 231610004459). The authors acknowledge Dr. Biplab Ghosh for his help in recording the XAS spectra (Indus-2, beamline 9) at RRCAT, Indore, India. The authors also acknowledge Indi Energy, Roorkee, India, for providing a free sample of hard carbon (BioBlackTM).

References

- [1] B. Dunn, H. Kamath, J.M. Tarascon, Electrical energy storage for the grid: A battery of choices, Science 334(6058) (2011) 928-935. https://doi.org/10.1126/science.1212741.
- [2] A. Manthiram, A reflection on lithium-ion battery cathode chemistry, Nat. Commun. 11(1) (2020) 1550. https://doi.org/10.1038/s41467-020-15355-0.
- [3] J.M. Tarascon, M. Armand, Issues and challenges facing rechargeable lithium batteries, Nature 414(6861) (2001) 359-367. https://doi.org/10.1038/35104644.
- [4] J.Y. Hwang, S.T. Myung, Y.K. Sun, Sodium-ion batteries: Present and future, Chem. Soc. Rev. 46(12) (2017) 3529-3614. https://doi.org/10.1039/c6cs00776g.
- [5] M. Chen, Q. Liu, S.-W. Wang, E. Wang, X. Guo, S.-L. Chou, High-Abundance and Low-Cost Metal-Based Cathode Materials for Sodium-Ion Batteries: Problems, Progress, and Key Technologies, Adv. Energy Mater. 9(14) (2019) 1803609. https://doi.org/10.1002/aenm.201803609.
- [6] V. Palomares, P. Serras, I. Villaluenga, K. Hueso, J. Gonzalez, T. Rojo, Na-ion Batteries, Recent Advances and Present Challenges to Become low Cost Energy Storage Systems, Energy Environ. Sci. 5 (2012) 5884-5901. https://doi.org/10.1039/C2EE02781J.
- [7] S. Wang, C. Sun, N. Wang, Q. Zhang, Ni- and/or Mn-based layered transition metal oxides as cathode materials for sodium ion batteries: status, challenges and countermeasures, J. Mater. Chem. A 7(17) (2019) 10138-10158. https://doi.org/10.1039/C8TA12441H.
- [8] C. Shi, L. Wang, X.a. Chen, J. Li, S. Wang, J. Wang, H. Jin, Challenges of layer-structured cathodes for sodium-ion batteries, Nanoscale Horizons 7(4) (2022) 338-351. https://doi.org/10.1039/D1NH00585E.
- [9] A. Sengupta, A. Kumar, G. Barik, A. Ahuja, J. Ghosh, H. Lohani, P. Kumari, T.K. Bhandakkar, S. Mitra, Lower Diffusion-Induced Stress in Nano-Crystallites of P2-Na_{2/3}Ni_{1/3}Mn_{1/2}Ti_{1/6}O₂ Novel Cathode for High Energy Na-ion Batteries, Small 19(12) (2023) 2206248. https://doi.org/https://doi.org/10.1002/smll.202206248.
- [10] C. Delmas, J.-J. Braconnier, C. Fouassier, P. Hagenmuller, Electrochemical intercalation of sodium in Na_xCoO₂ bronzes, Solid State Ion. 3-4 (1981) 165-169. https://doi.org/10.1016/0167-2738(81)90076-X.
- [11] C. Delmas, C. Fouassier, P. Hagenmuller, Structural classification and properties of the layered oxides, Physica B+C 99(1) (1980) 81-85. https://doi.org/10.1016/0378-4363(80)90214-4.
- [12] N. Yabuuchi, K. Kubota, M. Dahbi, S. Komaba, Research Development on Sodium-Ion Batteries, Chem. Rev. 114(23) (2014) 11636-11682. https://doi.org/10.1021/cr500192f.
- [13] L. Zhang, J. Wang, J. Li, G. Schuck, M. Winter, G. Schumacher, J. Li, Preferential occupation of Na in P3-type layered cathode material for sodium ion batteries, Nano Energy 70 (2020) 104535. https://doi.org/10.1016/j.nanoen.2020.104535.
- [14] C. Wu, Y. Xu, J. Song, Y. Hou, S. Jiang, R. He, A. Wei, Q. Tan, Research progress on P2-type layered oxide cathode materials for sodium-ion batteries, Chem. Eng. J. 500 (2024) 157264. https://doi.org/https://doi.org/10.1016/j.cej.2024.157264.
- [15] R.J. Clément, P.G. Bruce, C.P. Grey, Review—Manganese-Based P2-Type Transition Metal Oxides as Sodium-Ion Battery Cathode Materials, J. Electrochem. Soc. 162(14) (2015) A2589. https://doi.org/10.1149/2.0201514jes.
- [16] S. Saxena, M. Badole, H.N. Vasavan, V. Srihari, A.K. Das, P. Gami, S. Deswal, P. Kumar, S. Kumar, Deciphering the role of optimal P2/O3 phase fraction in enhanced cyclability and

- specific capacity of layered oxide cathodes, Chem. Eng. J. 485 (2024) 149921. https://doi.org/10.1016/j.cej.2024.149921.
- [17] R. Li, Y. Liu, Z. Wang, J. Li, A P2/O3 biphasic cathode material with highly reversibility synthesized by Sn-substitution for Na-ion batteries, Electrochim. Acta 318 (2019) 14-22. https://doi.org/10.1016/j.electacta.2019.06.020.
- [18] S. Saxena, H.N. Vasavan, M. Badole, A.K. Das, S. Deswal, P. Kumar, S. Kumar, Tailored P2/O3 phase-dependent electrochemical behavior of Mn-based cathode for sodium-ion batteries, J. Energy Storage 64 (2023) 107242. https://doi.org/https://doi.org/10.1016/j.est.2023.107242.
- [19] H.N. Vasavan, M. Badole, S. Saxena, V. Srihari, A.K. Das, P. Gami, S. Deswal, P. Kumar, S. Kumar, Impact of P3/P2 mixed phase on the structural and electrochemical performance of Na_{0.75}Mn_{0.75}Al_{0.25}O₂ cathode, J. Energy Storage 74 (2023) 109428. https://doi.org/https://doi.org/10.1016/j.est.2023.109428.
- [20] Y.N. Zhou, P.F. Wang, Y.B. Niu, Q. Li, X. Yu, Y.X. Yin, S. Xu, Y.G. Guo, A P2/P3 composite layered cathode for high-performance Na-ion full batteries, Nano Energy 55 (2019) 143-150. https://doi.org/10.1016/j.nanoen.2018.10.072.
- [21] S.-Y. Zhang, Y.-J. Guo, Y.-N. Zhou, X.-D. Zhang, Y.-B. Niu, E.-H. Wang, L.-B. Huang, P.-F. An, J. Zhang, X.-A. Yang, Y.-X. Yin, S. Xu, Y.-G. Guo, P3/O3 Integrated Layered Oxide as High-Power and Long-Life Cathode toward Na-Ion Batteries, Small 17(10) (2021) 2007236. https://doi.org/https://doi.org/10.1002/smll.202007236.
- [22] H.N. Vasavan, S. Saxena, V. Srihari, A.K. Das, P. Gami, N. Dagar, S. Deswal, P. Kumar, H.K. Poswal, S. Kumar, Elevating the Concentration of Na Ions to 1 in P2 Type Layered Oxide Cathodes, Adv. Funct. Mater. 35(20) (2025) 2421733. https://doi.org/https://doi.org/10.1002/adfm.202421733.
- [23] W. Zhang, K. Wang, H. Ning, Z. Qu, H. Luo, Q. Wei, P. Qing, X. Huang, X. Wang, G. Li, C. Huang, Z. Lan, W. Zhou, J. Guo, D. Huang, H. Liu, Nb-doped layered oxides with P2/O3 biphasic as high-rate, air-stable cathodes for sodium-ion batteries, J. Power Sources 635 (2025) 236516. https://doi.org/https://doi.org/10.1016/j.jpowsour.2025.236516.
- [24] H.N. Vasavan, M. Badole, S. Dwivedi, S. Kumar, Structural and transport properties of P2-Type Na_{0.70}Ni_{0.20}Cu_{0.15}Mn_{0.65}O₂ layered oxide, Ceram. Int. 48(s19) (2022) 28986-28993. https://doi.org/https://doi.org/10.1016/j.ceramint.2022.04.206.
- [25] H.N. Vasavan, M. Badole, S. Saxena, V. Srihari, A.K. Das, P. Gami, N. Dagar, S. Deswal, P. Kumar, H.K. Poswal, S. Kumar, Rational design of an optimal Al-substituted layered oxide cathode for Na-ion batteries, Electrochim. Acta 494 (2024) 144457. https://doi.org/https://doi.org/10.1016/j.electacta.2024.144457.
- [26] H.N. Vasavan, M. Badole, S. Saxena, V. Srihari, A.K. Das, P. Gami, S. Deswal, P. Kumar, S. Kumar, Unveiling the potential of P3 phase in enhancing the electrochemical performance of a layered oxide cathode, Mater. Today Energy 37 (2023) 101380. https://doi.org/10.1016/j.mtener.2023.101380.
- [27] J. Cabana, N.A. Chernova, J. Xiao, M. Roppolo, K.A. Aldi, M.S. Whittingham, C.P. Grey, Study of the Transition Metal Ordering in Layered NaxNix/2Mn1–x/2O2 ($2/3 \le x \le 1$) and Consequences of Na/Li Exchange, Inorg. Chem. 52(15) (2013) 8540-8550. https://doi.org/10.1021/ic400579w.
- [28] N. Dagar, S. Saxena, H.N. Vasavan, A.K. Das, P. Gami, S. Deswal, P. Kumar, K. Chinnathambi, V. Rathee, S. Kumar, Ti-Substitution Facilitating Anionic Redox and Cycle Stability in a P2-Type Na_{2/3}Mn_{2/3}Ni_{1/3}O₂ Na-Ion Battery Cathode, Energy & Fuels 39(6) (2025) 3348-3358. https://doi.org/10.1021/acs.energyfuels.4c05945.

- [29] W.L. Pang, X.H. Zhang, J.Z. Guo, J.Y. Li, X. Yan, B.H. Hou, H.Y. Guan, X.L. Wu, P2-type Na_{2/3}Mn_{1-x}Al_xO₂ cathode material for sodium-ion batteries: Al-doped enhanced electrochemical properties and studies on the electrode kinetics, J. Power Sources 356 (2017) 80-88. https://doi.org/10.1016/j.jpowsour.2017.04.076.
- [30] K. Kubota, T. Asari, S. Komaba, Impact of Ti and Zn Dual-Substitution in P2 Type Na_{2/3}Ni_{1/3}Mn_{2/3}O₂ on Ni–Mn and Na-Vacancy Ordering and Electrochemical Properties, Adv. Mater. 35(26) (2023) 2300714. https://doi.org/10.1002/adma.202300714.
- [31] H. Yi, Z. Li, X. Li, P. Gao, Y. Zhu, Ti-Substituted O3-NaNi_{0.5}Mn_{0.3}Ti_{0.2}O₂ Material with a Disordered Transition Metal Layer and a Stable Structure, ACS Appl. Mater. Interfaces 16(33) (2024) 43636-43646. https://doi.org/10.1021/acsami.4c08777.
- [32] H.N. Vasavan, M. Badole, S. Dwivedi, D. Kumar, P. Kumar, S. Kumar, Enhanced rate performance and specific capacity in Ti-substituted P2-type layered oxide enabled by crystal structure and particle morphology modifications, Chem. Eng. J. 448 (2022) 137662. https://doi.org/10.1016/j.cej.2022.137662.
- [33] P.K. Nayak, J. Grinblat, M. Levi, E. Levi, S. Kim, J.W. Choi, D. Aurbach, Al Doping for Mitigating the Capacity Fading and Voltage Decay of Layered Li and Mn-Rich Cathodes for Li-Ion Batteries, Adv. Energy Mater. 6(8) (2016) 1502398. https://doi.org/10.1002/aenm.201502398.
- [34] X. Liu, G. Zhong, Z. Xiao, B. Zheng, W. Zuo, K. Zhou, H. Liu, Z. Liang, Y. Xiang, Z. Chen, G.F. Ortiz, R. Fu, Y. Yang, Al and Fe-containing Mn-based layered cathode with controlled vacancies for high-rate sodium ion batteries, Nano Energy 76 (2020). https://doi.org/10.1016/j.nanoen.2020.104997.
- [35] L. Gao, J.-N. Yang, Q. Zheng, Y. Zhang, X. Jiang, S.-Q. Li, J.-S. Chen, K.-X. Wang, Stable layered oxide cathode materials with ultra-low volume change for high-performance sodium-ion batteries, Chem. Eng. J. 510 (2025) 161580. https://doi.org/10.1016/j.cej.2025.161580.
- [36] T. Park, J. Jeong, S. Kang, J. Kim, K. Min, Revealing the role of dopants to suppress phase transition in biphasic layered transition metal oxide cathodes for sodium-ion batteries, J. Power Sources 640 (2025) 236718. https://doi.org/https://doi.org/10.1016/j.jpowsour.2025.236718.
- [37] T. Yang, Y. Huang, J. Zhang, H. Zhu, J. Ren, T. Li, L.C. Gallington, S. Lan, L. Yang, Q. Liu, Insights into Ti doping for stabilizing the Na_{2/3}Fe_{1/3}Mn_{2/3}O₂ cathode in sodium ion battery, J. Energy Chem. 73 (2022) 542-548. https://doi.org/https://doi.org/10.1016/j.jechem.2022.06.016.
- [38] C. Cheng, M. Ding, T. Yan, J. Jiang, J. Mao, X. Feng, T.S. Chan, N. Li, L. Zhang, Anionic Redox Activities Boosted by Aluminum Doping in Layered Sodium-Ion Battery Electrode, Small Methods 6(3) (2022). https://doi.org/10.1002/smtd.202101524.
- [39] D.-W. Han, J.-H. Ku, R.-H. Kim, D.-J. Yun, S.-S. Lee, S.-G. Doo, Aluminum Manganese Oxides with Mixed Crystal Structure: High-Energy-Density Cathodes for Rechargeable Sodium Batteries, ChemSusChem 7(7) (2014) 1870-1875. https://doi.org/10.1002/cssc.201301254.
- [40] S. Saxena, H.N. Vasavan, N. Dagar, V. Srihari, A.K. Das, P. Gami, S. Deswal, P. Kumar, H.K. Poswal, S. Kumar, Strategic phase modulation in Na_{0.8}(Mn-Fe-Ni)O₂ system delivers high energy density and structural stability, J. Power Sources 644 (2025) 237115. https://doi.org/https://doi.org/10.1016/j.jpowsour.2025.237115.
- [41] M. Jia, H. Li, Y. Qiao, L. Wang, X. Cao, J. Cabana, H. Zhou, Elucidating Anionic Redox Chemistry in P3 Layered Cathode for Na-Ion Batteries, ACS Appl. Mater. Interfaces 12(34) (2020) 38249-38255. https://doi.org/10.1021/acsami.0c11763.

- [42] C. Zhao, Q. Wang, Z. Yao, J. Wang, B. Sánchez-Lengeling, F. Ding, X. Qi, Y. Lu, X. Bai, B. Li, H. Li, A. Aspuru-Guzik, X. Huang, C. Delmas, M. Wagemaker, L. Chen, Y.-S. Hu, Rational design of layered oxide materials for sodium-ion batteries, Science 370(6517) (2020) 708-711. https://doi.org/10.1126/science.aay9972.
- [43] A. Coelho, TOPAS and TOPAS-Academic: an optimization program integrating computer algebra and crystallographic objects written in C++, J. Appl. Crystallogr. 51(1) (2018) 210-218. https://doi.org/10.1107/S1600576718000183.
- [44] H.N. Vasavan, M. Badole, S. Saxena, V. Srihari, A.K. Das, P. Gami, N. Dagar, S. Deswal, P. Kumar, H.K. Poswal, S. Kumar, Identification of optimal composition with superior electrochemical properties along the zero Mn³⁺ line in Na_{0.75}(Mn-Al-Ni)O₂ pseudo ternary system, J. Energy Chem. 96 (2024) 206-216. https://doi.org/https://doi.org/10.1016/j.jechem.2024.04.015.
- [45] T.L. Cottrell, The Strengths of Chemical Bonds, Academic Press1954.
- [46] W. Kang, D.Y.W. Yu, P.-K. Lee, Z. Zhang, H. Bian, W. Li, T.-W. Ng, W. Zhang, C.-S. Lee, P2-Type Na_xCu_{0.15}Ni_{0.20}Mn_{0.65}O₂ Cathodes with High Voltage for High-Power and Long-Life Sodium-Ion Batteries, ACS Appl. Mater. Interfaces 8(46) (2016) 31661-31668. https://doi.org/10.1021/acsami.6b10841.
- [47] H.N. Vasavan, M. Badole, S. Saxena, A.K. Das, S. Deswal, P. Kumar, S. Kumar, Excellent Structural Stability-Driven Cyclability in P2-Type Ti-Based Cathode for Na-Ion Batteries, ACS Appl. Energy Mater. 6(4) (2023) 2440-2447. https://doi.org/10.1021/acsaem.2c03750.
- [48] J. Xu, D.H. Lee, R.J. Clément, X. Yu, M. Leskes, A.J. Pell, G. Pintacuda, X.-Q. Yang, C.P. Grey, Y.S. Meng, Identifying the Critical Role of Li Substitution in P2–Na_x[Li_yNi_zMn_{1–y-z}]O₂ (0 < x, y, z < 1) Intercalation Cathode Materials for High-Energy Na-Ion Batteries, Chem. Mater. 26(2) (2014) 1260-1269. https://doi.org/10.1021/cm403855t.
- [49] Q. Liu, Z. Hu, M. Chen, C. Zou, H. Jin, S. Wang, S.-L. Chou, S.-X. Dou, Recent Progress of Layered Transition Metal Oxide Cathodes for Sodium-Ion Batteries, Small 15(32) (2019) 1805381. https://doi.org/10.1002/smll.201805381.
- [50] C. Li, F. Geng, B. Hu, B. Hu, Anionic redox in Na-based layered oxide cathodes: a review with focus on mechanism studies, Mater. Today Energy 17 (2020) 100474. https://doi.org/10.1016/j.mtener.2020.100474.
- [51] P.F. Wang, H.R. Yao, X.Y. Liu, Y.X. Yin, J.N. Zhang, Y. Wen, X. Yu, L. Gu, Y.G. Guo, Na⁺/vacancy disordering promises high-rate Na-ion batteries, Sci. Adv. 4(3) (2018) eaar6018. https://doi.org/10.1126/sciadv.aar6018.
- [52] C.-H. Yeh, J.-W. Kang, Y.-L. Chen, H.-J. Chen, H.-H. Chang, W.-H. Lu, S.-Y. Chen, H.-L. Chen, C.-W. Hu, L.-Y. Chueh, Y.-T.F. Pan, H.-Y. Chen, Electrochemical Improvement of Na_{0.62}K_{0.05}Mg_{2/9}Cu_{1/9}Mn_{2/3}O₂ P2-Type Layer-Oxide Anionic Redox Cathodes of Sodium-Ion Batteries via Incorporating K-Doping, ACS Sustain. Chem. Eng. 12(34) (2024) 12795-12807. https://doi.org/10.1021/acssuschemeng.4c03148.
- [53] Z.-Y. Xie, X. Xing, L. Yu, Y.-X. Chang, Y.-X. Yin, L. Xu, M. Yan, S. Xu, Mg/Ti doping co-promoted high-performance P2-Na_{0.67}Ni_{0.28}Mg_{0.05}Mn_{0.62}Ti_{0.05}O₂ for sodium-ion batteries, Appl. Phys. Lett. 121(20) (2022) 203903. https://doi.org/10.1063/5.0121824.
- [54] X. Zhang, H. Chen, S. Xu, M. Zhou, R. Nie, Y. Yang, C. Li, H. Zhou, Zinc-substituted P2-type Na_{0.67}Ni_{0.23}Zn_{0.1}Mn_{0.67}O₂ cathode with improved rate capability and cyclic stability for sodium-ion storage at high voltage, J. Alloys Compd. 968 (2023) 172190. https://doi.org/10.1016/j.jallcom.2023.172190.
- [55] F. Fu, X. Liu, X. Fu, H. Chen, L. Huang, J. Fan, J. Le, Q. Wang, W. Yang, Y. Ren, K. Amine, S.-G. Sun, G.-L. Xu, Entropy and crystal-facet modulation of P2-type layered

- cathodes for long-lasting sodium-based batteries, Nat. Commun. 13(1) (2022) 2826. https://doi.org/10.1038/s41467-022-30113-0.
- [56] E. Grépin, Y. Zhou, B. Li, G. Rousse, J.-M. Tarascon, S. Mariyappan, Optimal Ti-Substitution in Layered Oxide Cathodes for Na-Ion Batteries, Chem. Mater. 36(21) (2024) 10804-10812. https://doi.org/10.1021/acs.chemmater.4c02501.
- [57] Y. You, S. Xin, H.Y. Asl, W. Li, P.-F. Wang, Y.-G. Guo, A. Manthiram, Insights into the Improved High-Voltage Performance of Li-Incorporated Layered Oxide Cathodes for Sodium-Ion Batteries, Chem 4(9) (2018) 2124-2139. https://doi.org/10.1016/j.chempr.2018.05.018.
- [58] L.-R. Wu, Y.-H. Zhang, Z. Wu, J. Tian, H. Wang, H. Zhao, S. Xu, L. Chen, X. Duan, D. Zhang, H. Guo, Y. You, Z. Zhu, Stabilized O3-Type Layered Sodium Oxides with Enhanced Rate Performance and Cycling Stability by Dual-Site Ti⁴⁺/K⁺ Substitution, Adv. Sci. 10(32) (2023) 2304067. https://doi.org/10.1002/advs.202304067.
- [59] Y.-J. Guo, R.-X. Jin, M. Fan, W.-P. Wang, S. Xin, L.-J. Wan, Y.-G. Guo, Sodium layered oxide cathodes: properties, practicality and prospects, Chem. Soc. Rev. 53(15) (2024) 7828-7874. https://doi.org/10.1039/D4CS00415A.
- [60] W. Zuo, A. Innocenti, M. Zarrabeitia, D. Bresser, Y. Yang, S. Passerini, Layered Oxide Cathodes for Sodium-Ion Batteries: Storage Mechanism, Electrochemistry, and Technoeconomics, Acc. Chem. Res. 56(3) (2023) 284-296. https://doi.org/10.1021/acs.accounts.2c00690.
- [61] Y.-E. Zhu, X. Qi, X. Chen, X. Zhou, X. Zhang, J. Wei, Y. Hu, Z. Zhou, A P2-Na_{0.67}Co_{0.5}Mn_{0.5}O₂ cathode material with excellent rate capability and cycling stability for sodium ion batteries, J. Mater. Chem. A 4(28) (2016) 11103-11109. https://doi.org/10.1039/C6TA02845D.
- [62] X. Qi, Y. Wang, L. Jiang, L. Mu, C. Zhao, L. Liu, Y.-S. Hu, L. Chen, X. Huang, Sodium-Deficient O3-Na_{0.9}[Ni_{0.4}Mn_xTi_{0.6-x}]O₂ Layered-Oxide Cathode Materials for Sodium-Ion Batteries, Particle & Particle Systems Characterization 33(8) (2016) 538-544. https://doi.org/10.1002/ppsc.201500129.
- [63] S. Komaba, N. Yabuuchi, T. Nakayama, A. Ogata, T. Ishikawa, I. Nakai, Study on the Reversible Electrode Reaction of $Na_{1-x}Ni_{0.5}Mn_{0.5}O_2$ for a Rechargeable Sodium-Ion Battery, Inorg. Chem. 51 (2012) 6211-20. https://doi.org/10.1021/ic300357d.
- [64] X. Dou, I. Hasa, D. Saurel, C. Vaalma, L. Wu, D. Buchholz, D. Bresser, S. Komaba, S. Passerini, Hard carbons for sodium-ion batteries: Structure, analysis, sustainability, and electrochemistry, Mater. Today 23 (2019) 87-104. https://doi.org/10.1016/j.mattod.2018.12.040.
- [65] X. Cao, X. Li, Y. Qiao, M. Jia, F. Qiu, Y. He, P. He, H. Zhou, Restraining Oxygen Loss and Suppressing Structural Distortion in a Newly Ti-Substituted Layered Oxide P2-Na_{0.66}Li_{0.22}Ti_{0.15}Mn_{0.63}O₂, ACS Energy Lett. 4(10) (2019) 2409-2417. https://doi.org/10.1021/acsenergylett.9b01732.
- [66] C. Li, C. Zhao, B. Hu, W. Tong, M. Shen, B. Hu, Unraveling the Critical Role of Ti Substitution in P2-Na_xLi_yMn_{1-y}O₂ Cathodes for Highly Reversible Oxygen Redox Chemistry, Chem. Mater. 32(3) (2020) 1054-1063. https://doi.org/10.1021/acs.chemmater.9b03765.
- [67] Y. Li, K.A. Mazzio, N. Yaqoob, Y. Sun, A.I. Freytag, D. Wong, C. Schulz, V. Baran, A.S.J. Mendez, G. Schuck, M. Zając, P. Kaghazchi, P. Adelhelm, Competing Mechanisms Determine Oxygen Redox in Doped Ni–Mn Based Layered Oxides for Na-Ion Batteries, Adv. Mater. 36(18) (2024) 2309842. https://doi.org/https://doi.org/10.1002/adma.202309842.

[Supplementary Materials]

Biphasic P3/O3 driven excellent electrochemical behavior and structural stability in a dual pillar-ions sodium layered oxide cathode

Neha Dagar¹, Samriddhi Saxena¹, Velaga Srihari², Himanshu Kumar Poswal², Sonia Deswal³, Pradeep Kumar³, and Sunil Kumar^{1,*}

¹Department of Metallurgical Engineering and Materials Science, Indian Institute of Technology Indore, Simrol, 453552, India

²High Pressure & Synchrotron Radiation Physics Division, Bhabha Atomic Research Centre, Mumbai, 400085, India.

³School of Physical Sciences, Indian Institute of Technology Mandi, Mandi, 175005, India *sunil@iiti.ac.in

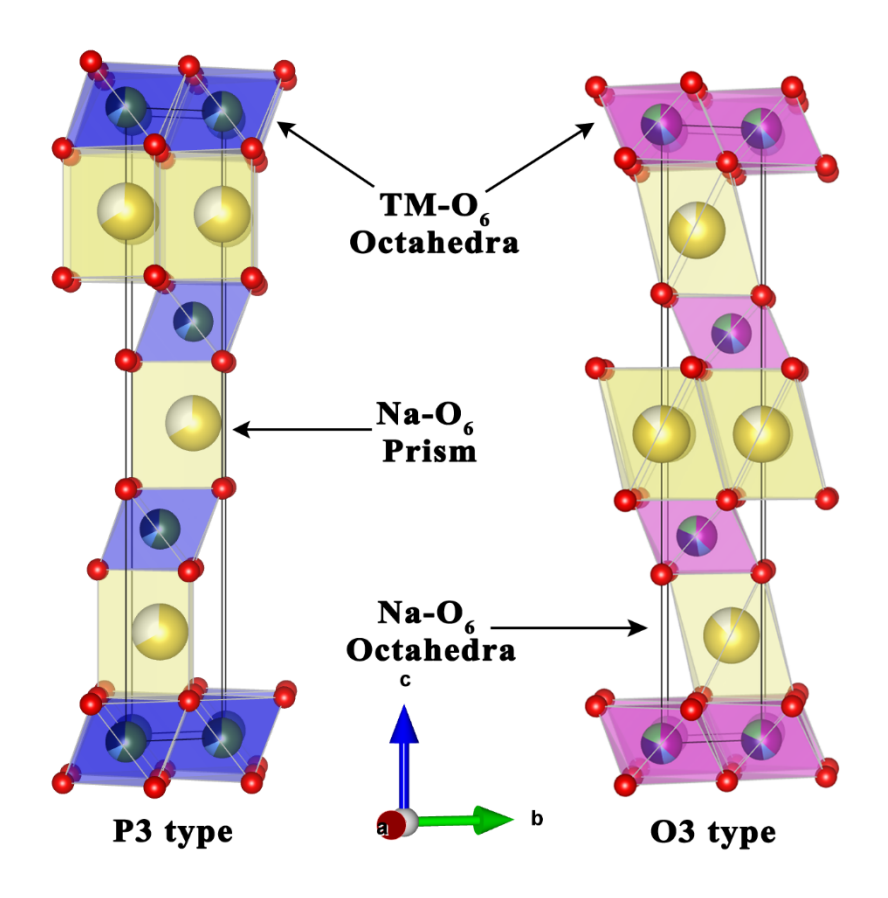


Fig. S1: Schematics of P3 and O3 type structures.

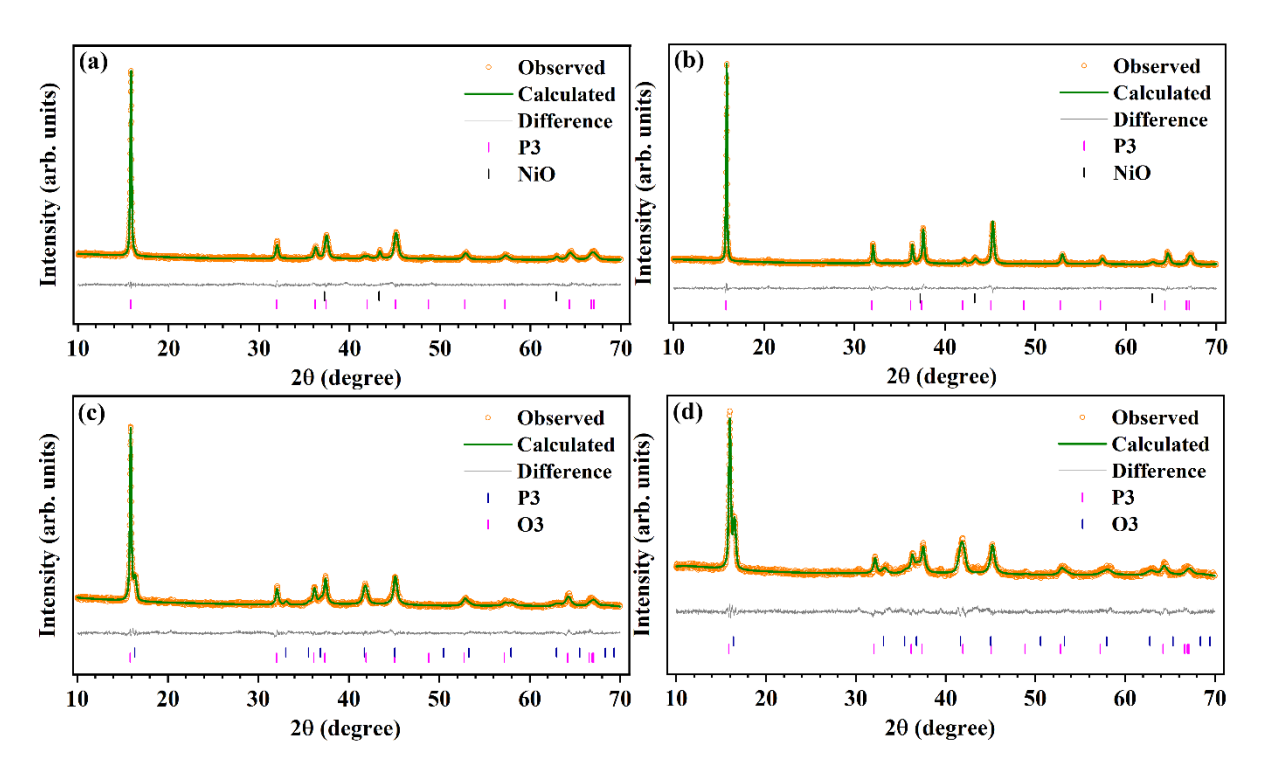


Fig. S2: Rietveld refinement profiles for (a) NMAT-0, (b) NMAT-05, (c) NMAT-15, and (d) NMAT-20.

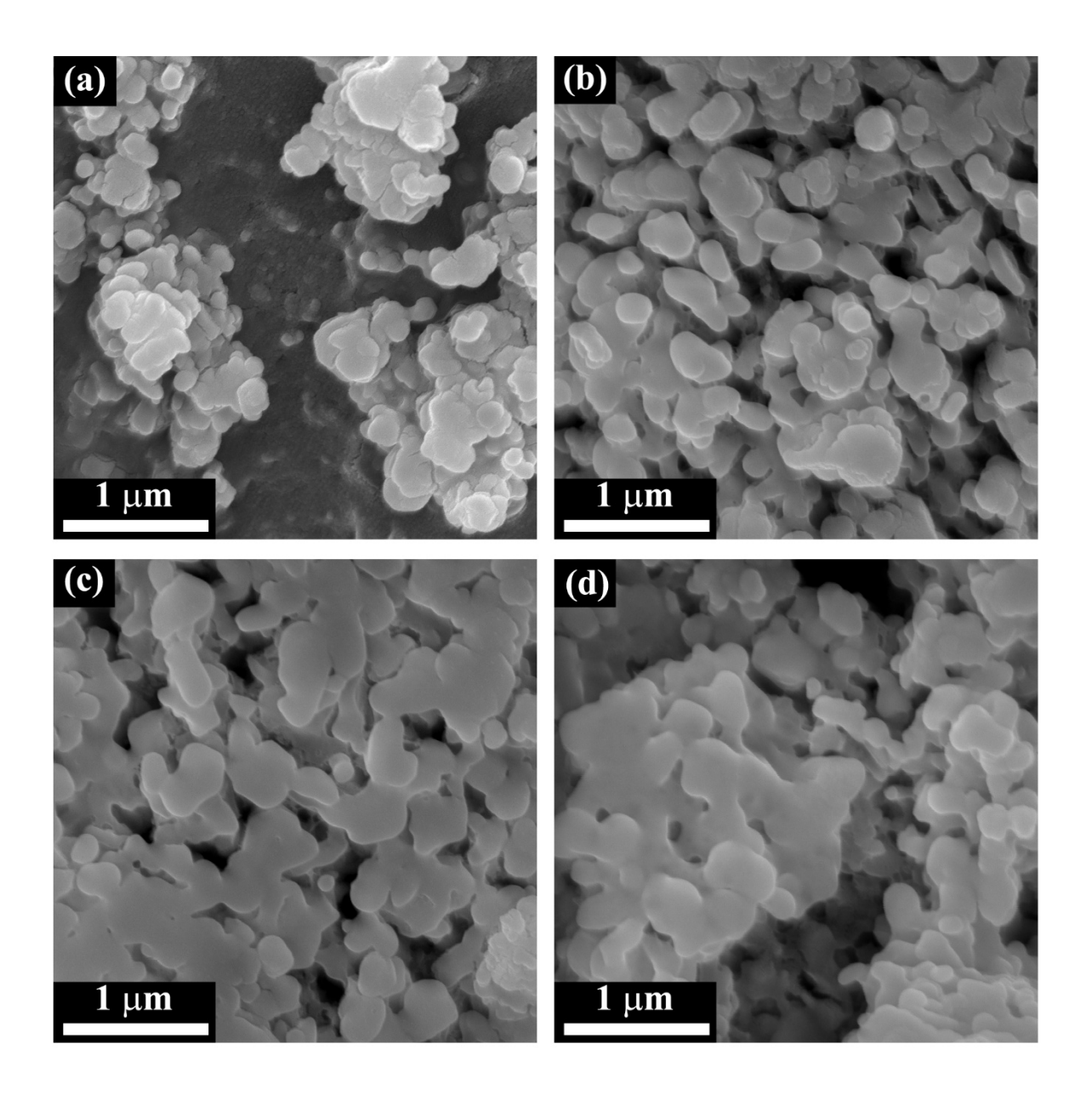


Fig. S3: SEM images of (a) NMAT-0, (b) NMAT-05, (c) NMAT-15, and (d) NMAT-20 samples.

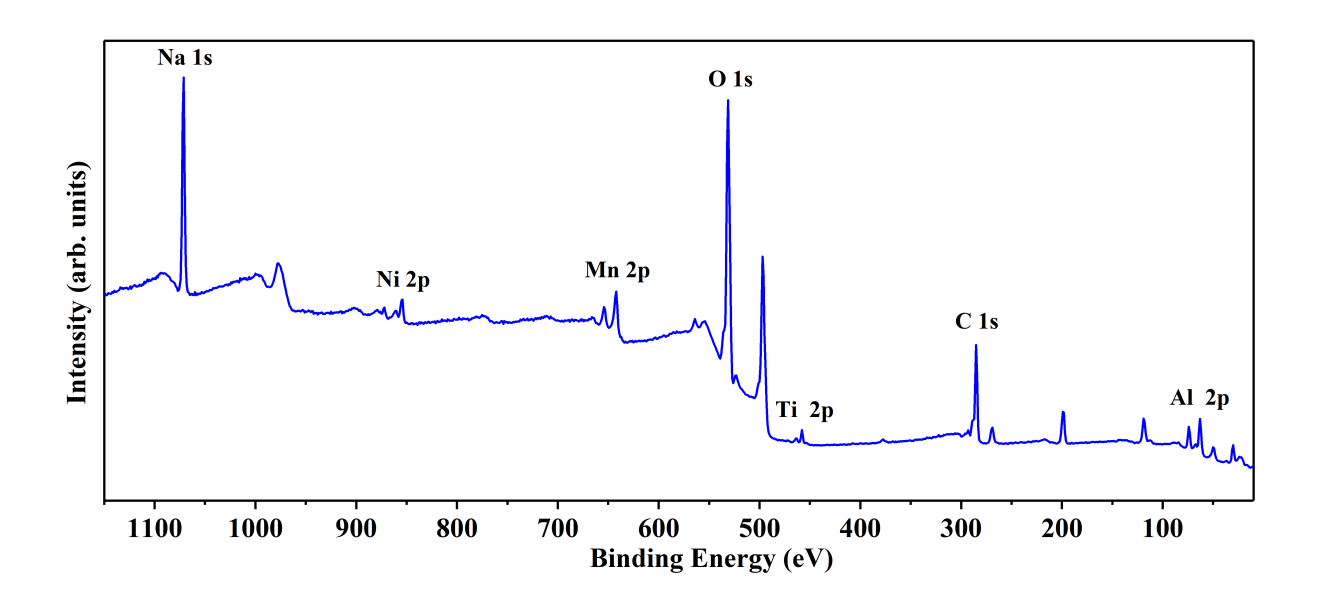


Fig. S4: XPS survey scan of NMAT-10 sample.

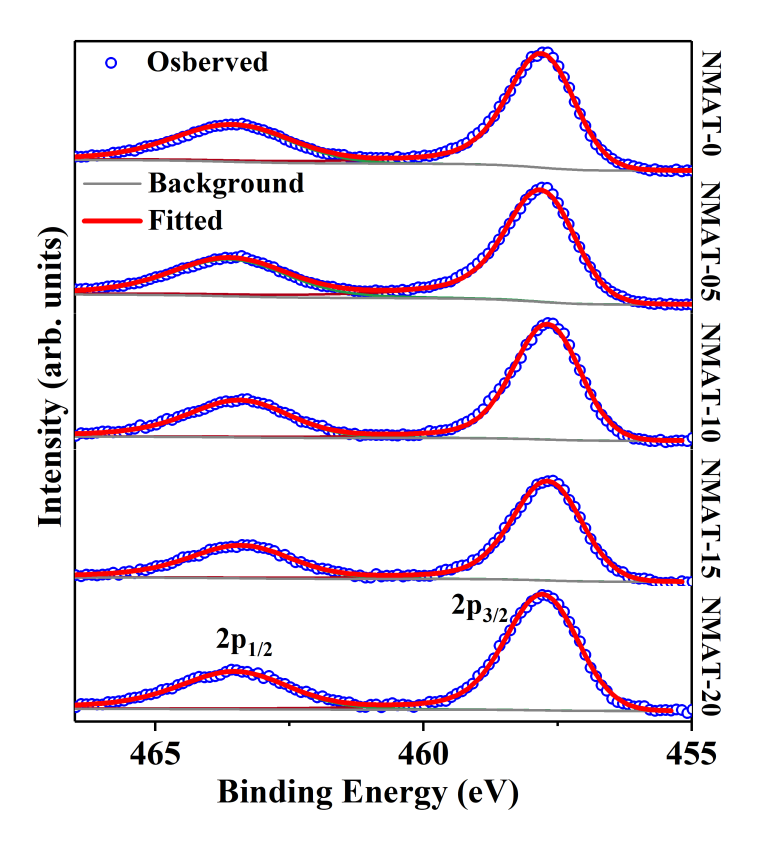


Fig. S5: Experimental and fitted XPS data for Ti 2p for NMAT samples.

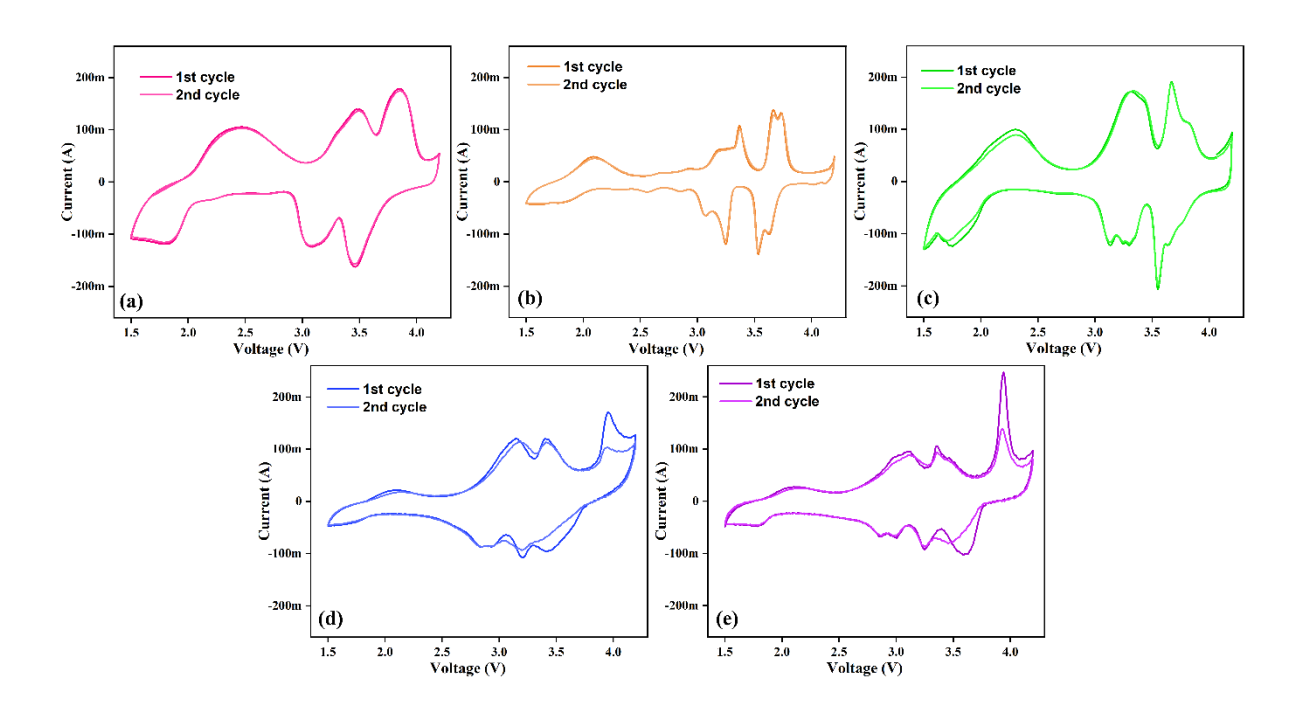


Fig. S6: CV curves at a scan rate of 0.1 mV s^{-1} of (a) NMAT-0, (b) NMAT-05, (c) NMAT-10, (d) NMAT-15, and (e) NMAT-20.

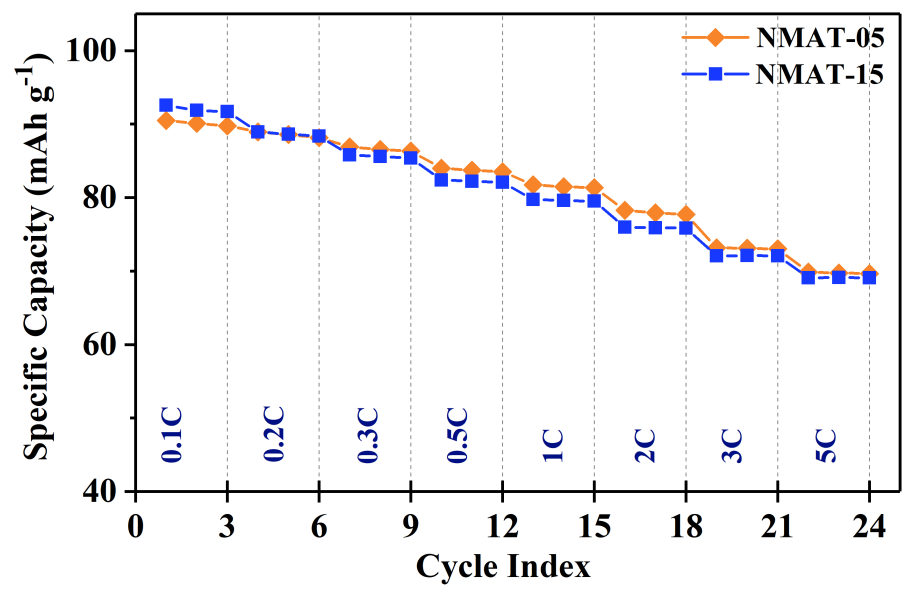


Fig. S7: Discharge-specific capacity at various C-rates for NMAT-05 and NMAT-15 samples in the 2.0-4.2 V range.

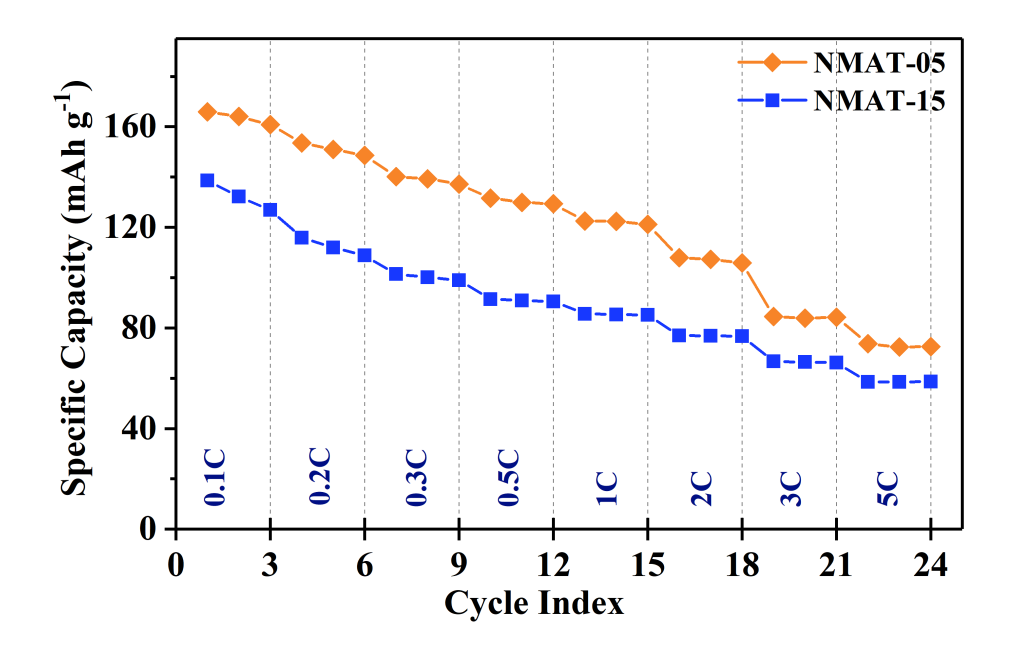


Fig. S8: Discharge-specific capacity at various C-rates for NMAT-05 and NMAT-15 samples in the 1.5-4.2 V range.

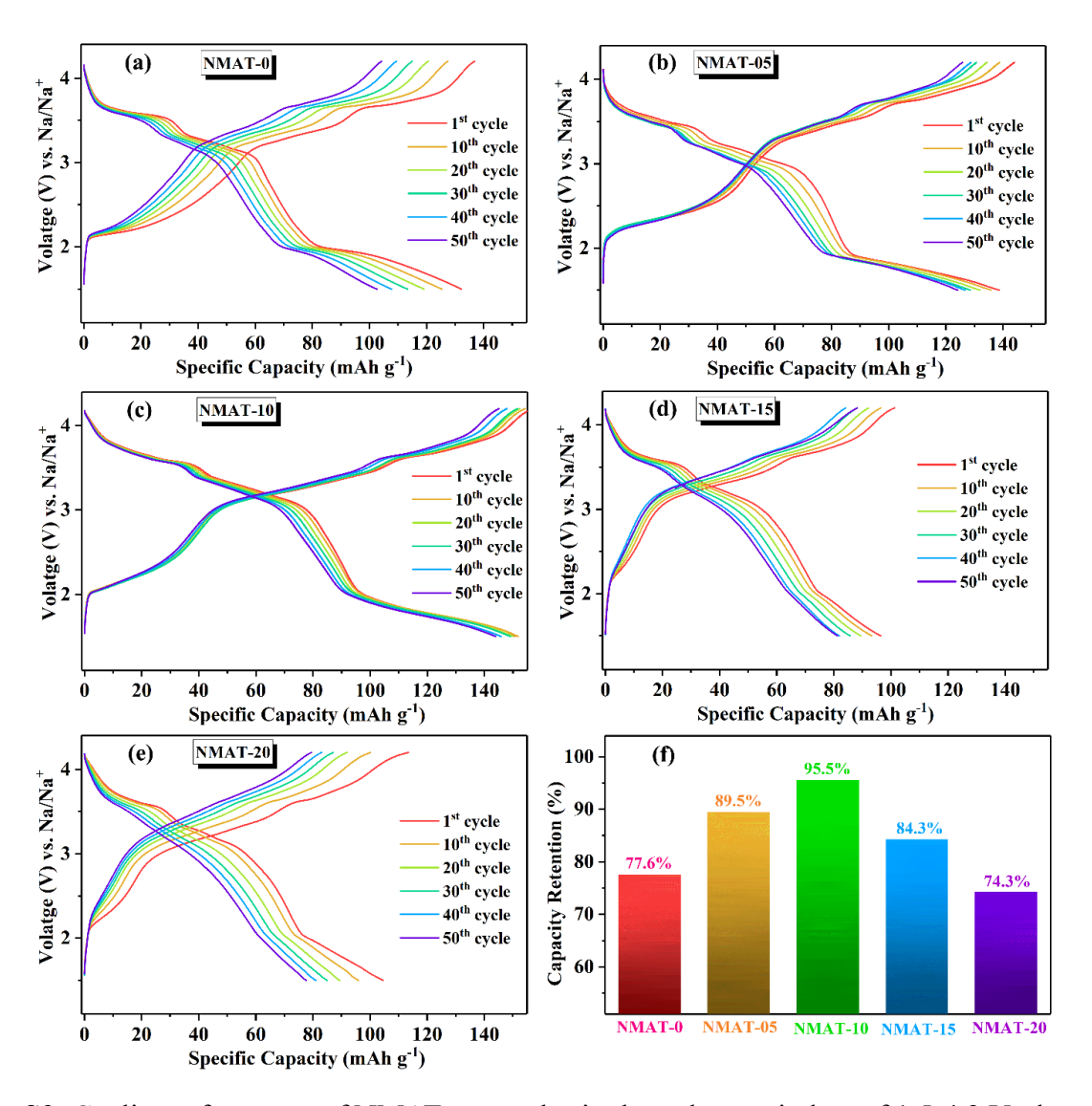


Fig. S9: Cyclic performance of NMAT-x samples in the voltage window of 1.5-4.2 V, along with the capacity retention plot (f).

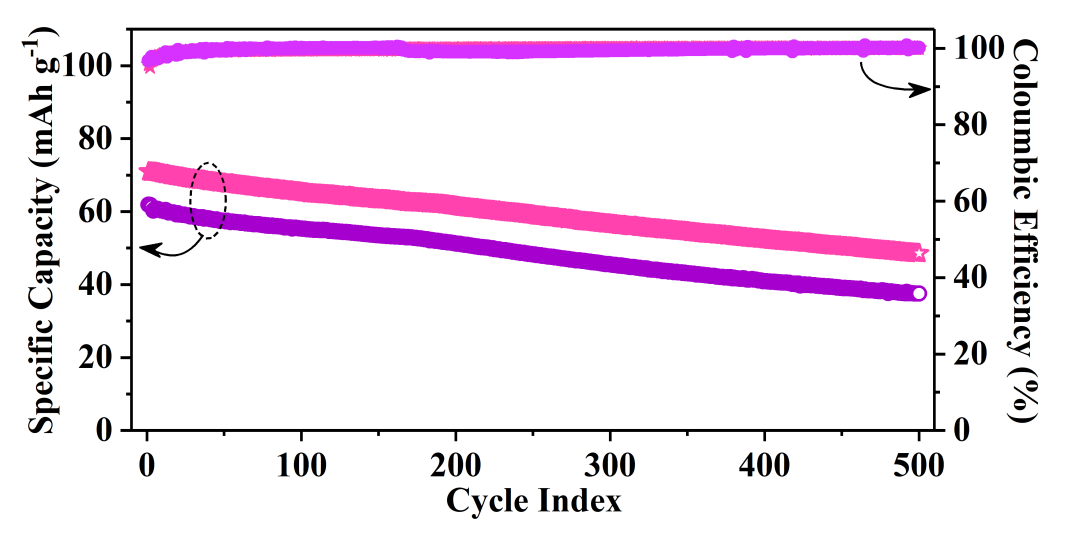


Fig. S10: Cycling performance of NMAT-0 and NMAT-20 at 2C.

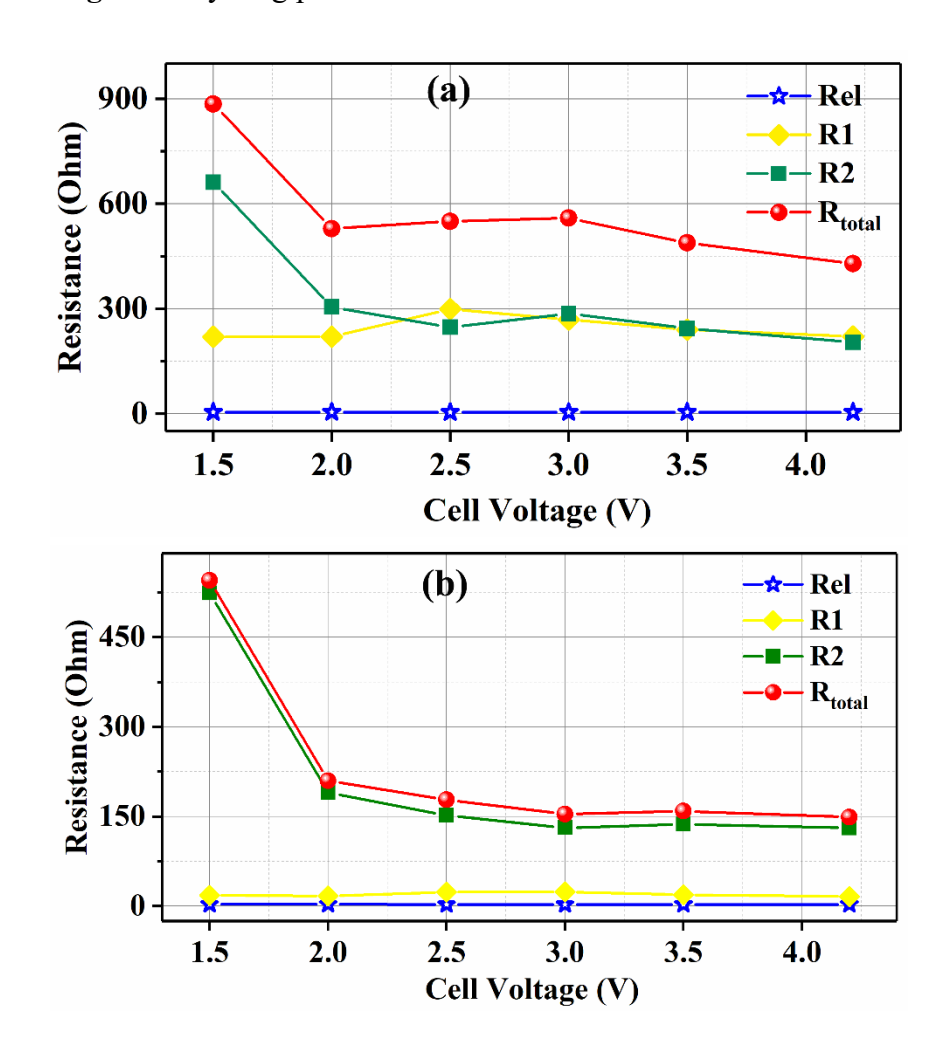


Fig. S11: Values of various resistances for (a) NMAT-0 and (b) NMAT-10 cells.

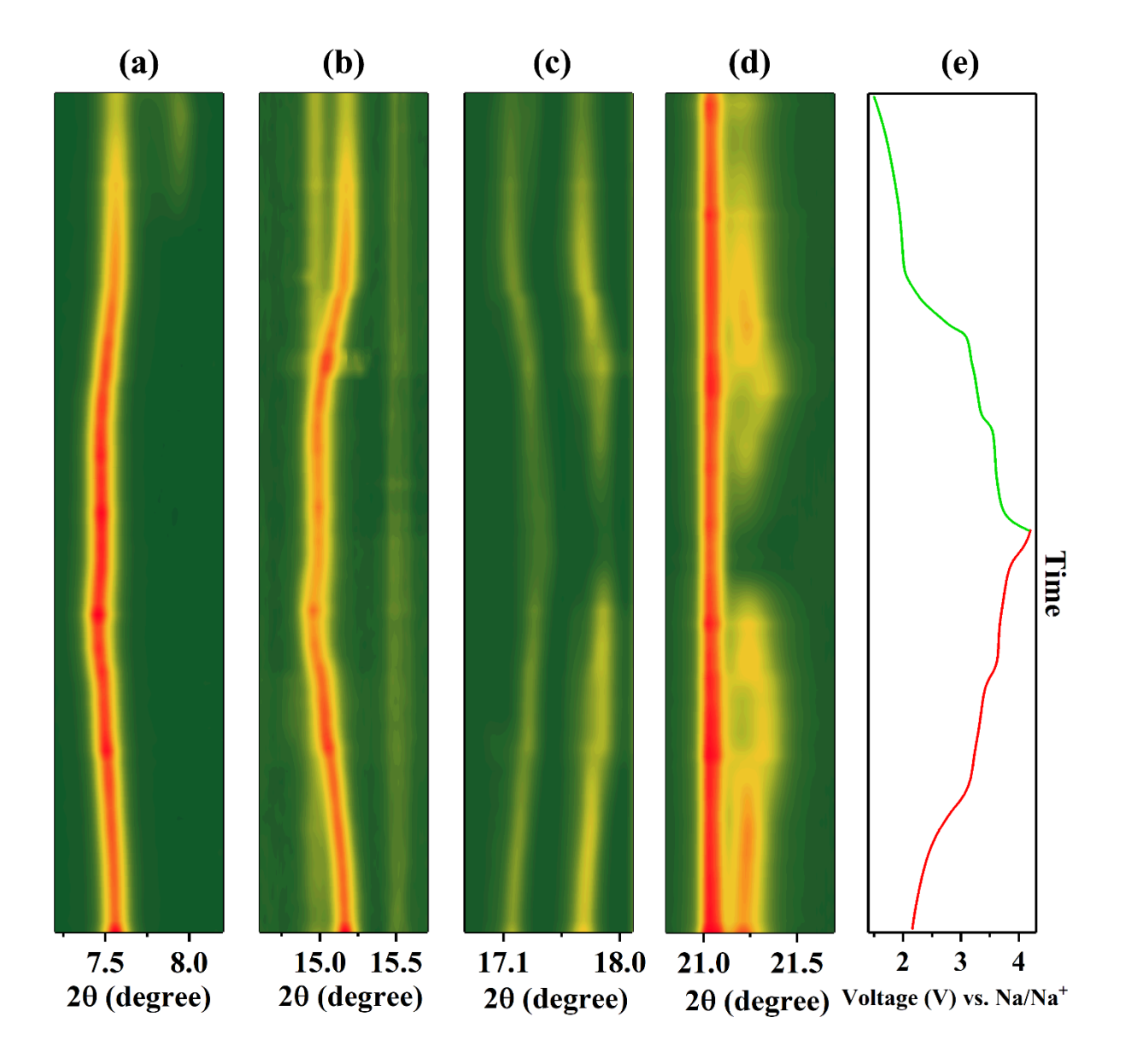


Fig. S12: Contour plots of the *operando* synchrotron XRD data for selected peaks (a) P3(003), (b) P3(006), (c) P3(101)/P3(102), and (d) P3(105) during the charge-discharge process (shown in panel (e)) for the NMAT-0 cathode.

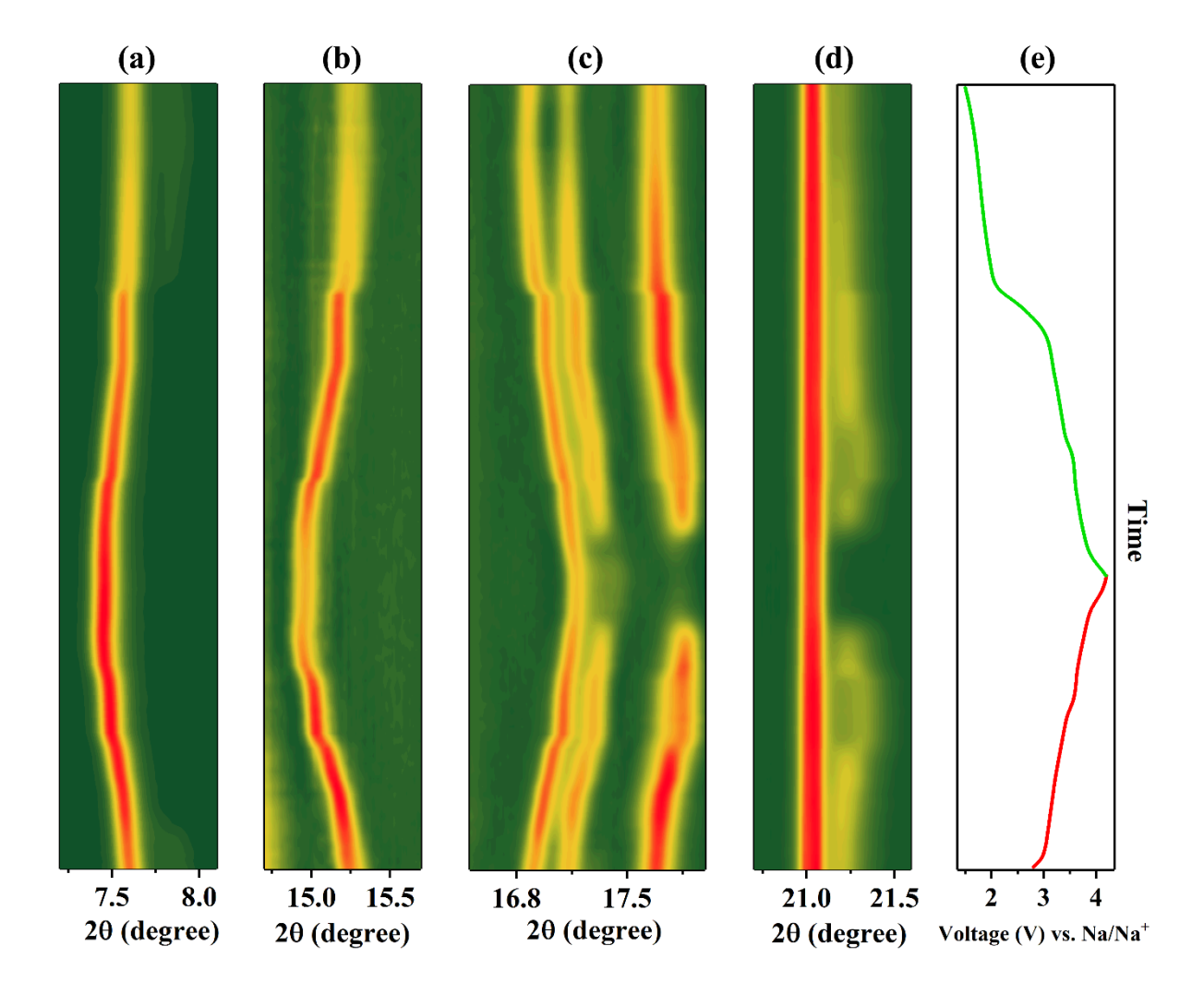


Fig. S13: Contour plots of the *operando* synchrotron XRD data for selected peaks (a) P3(003), (b) P3(006), (c) O3(101)/P3(101)/P3(102), and (d) P3(105) during the charge-discharge process (shown in panel (e)) for the NMAT-10 cathode.

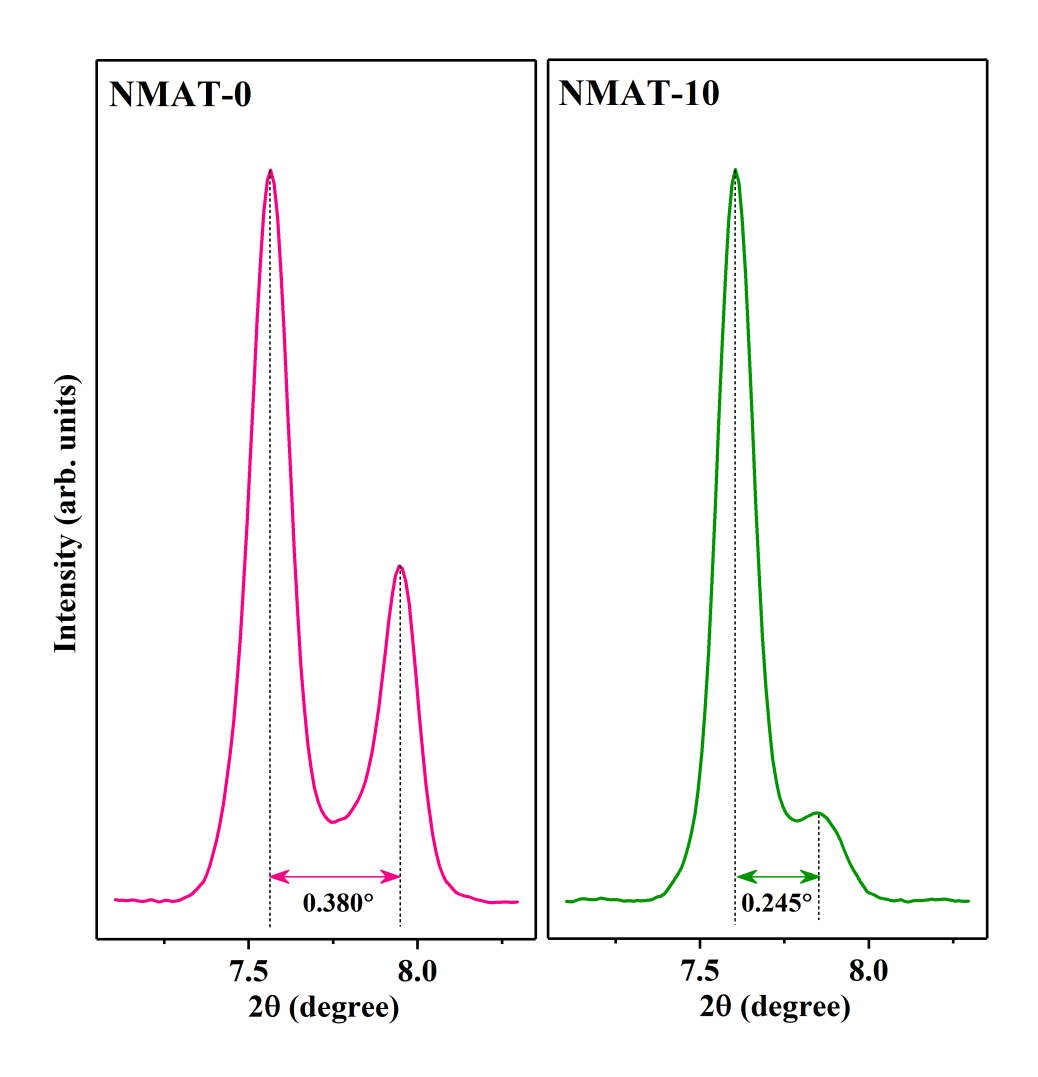


Fig. S14: XRD patterns illustrating the P3 (003) and O3 (003) peaks in both NMAT-0 and NMAT-10 samples discharged to 1.5 V.

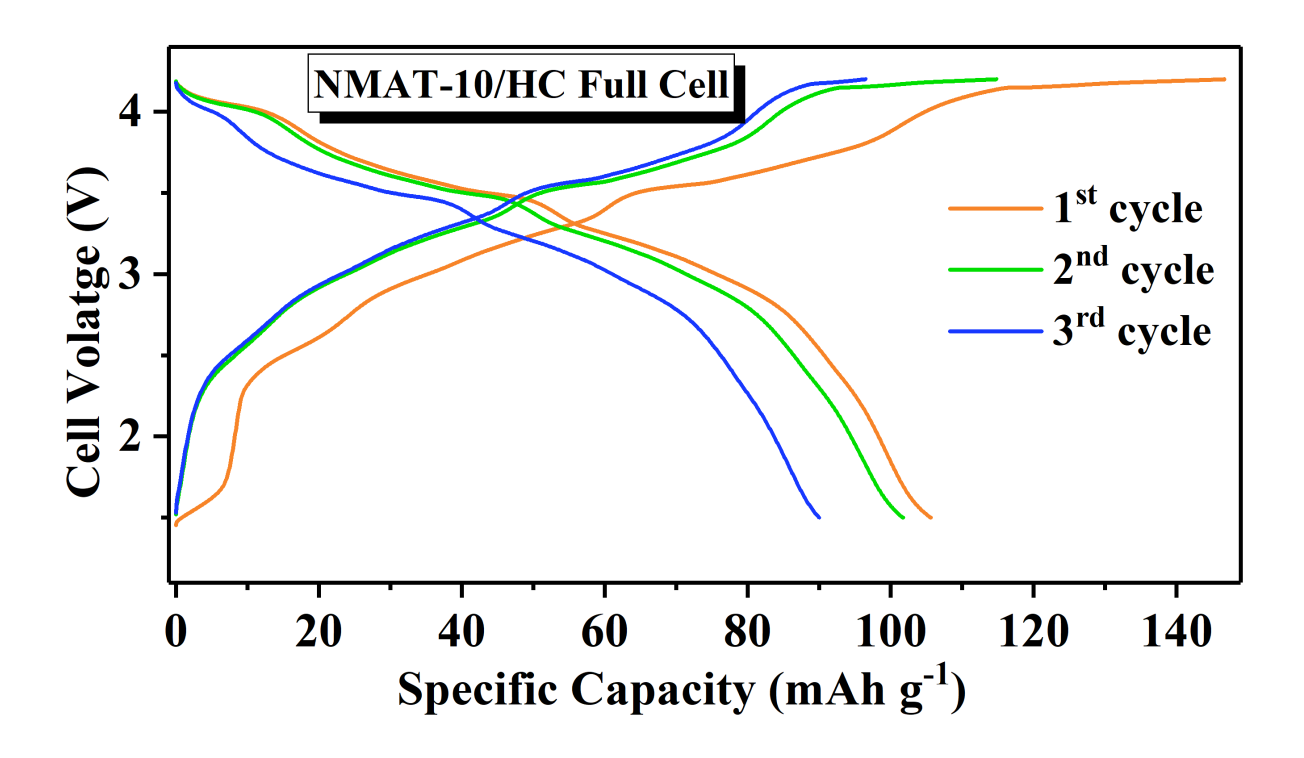


Fig. S15: Cell voltage versus specific capacity for NMAT-10 and hard carbon cell at 0.2C in the 1.5-4.2 V range.

Table S1: Various structural parameters obtained from the Rietveld refinement of room temperature powder x-ray diffraction data for NMAT-x samples. x, y, z — positional coordinates along with the fitness parameters (Rexp, Rwp, Rp, and goodness of fit – GoF).

	1	T		1		1
NMAT-0		Atom	x	y	z	Occupancy
$R_{exp} = 2.17$	Р3	Na	0	0	0.177	0.67
$R_{wp} = 2.61$		Mn/ Ti/ Ni	0	0	0	0.57/0.10/0.33
$R_p = 2.04$		O1	0	0	0.389	1
GOF = 1.21		O2	0	0	-0.389	1
NMAT-05		Atom	х	у	z	Occupancy
$R_{exp} = 2.08$		Na	0	0	0.170	0.72
$R_{wp}=2.57$	Р3	Mn/ Ti/ Ni/ Al	0	0	0	0.52/0.10/033/0.05
$R_p = 2.01$		O1	0	0	0.395	1
GOF = 1.23		O2	0	0	-0.395	1
		Atom	х	у	z	Occupancy
		Na	0	0	0.172	0.77
NMAT-10	Р3	Mn/ Ti/ Ni/ Al	0	0	0	0.47/0.10/0.33/0.10
$R_{exp} = 2.45$		O1	0	0	0.398	1
$R_{wp} = 3.03$		O2	0	0	-0.398	1
$R_p = 2.38$	О3	Atom	х	у	z	Occupancy
GOF = 1.24		Na	0	0	0.5	0.77
		Mn/ Ti/ Ni/ Al	0	0	0	0.47/0.10/0.33/0.10
		0	0	0	0.261	1
		Atom	x	у	z	Occupancy
		Na	0	0	0.171	0.82
NMAT-15	Р3	Mn/ Ti/ Ni/ Al	0	0	0	0.42/0.10/0.33/0.15
$R_{exp} = 2.33$		O1	0	0	0.398	1
$R_{wp} = 2.98$		O2	0	0	-0.398	1
$R_p = 2.33$		Atom	x	у	z	Occupancy
GOF = 1.28	02	Na	0	0	0.5	0.82
	О3	Mn/ Ti/ Ni/ Al	0	0	0	0.42/0.10/0.33/0.15
		0	0	0	0.271	1
NMAT-20		Atom	x	y	z	Occupancy
$R_{exp} = 2.46$	P3	Na	0	0	0.180	0.87
$R_{wp}=3.42$		Mn/ Ti/ Ni/ Al	0	0	0	0.37/0.10/0.33/0.20
	1	l .			1	t

$R_p = 2.69$ GOF = 1.39		O1	0	0	0.402	1
GOF = 1.39		O2	0	0	-0.402	1
		Atom	x	у	z	Occupancy
	03	Na	0	0	0.5	0.87
	US	Mn/ Ti/ Ni/ Al	0	0	0	0.37/0.10/0.33/0.20
		0	0	0	0.270	1

Table S2. The weight (%) of various elements in NMAT-*x* samples determined from the ICP-OES measurements.

Sample	Na (wt.%)	Mn (wt.%)	Al (wt.%)	Ni (wt.%)	Ti (wt.%)	Chemical Composition
NMAT-0	21.47	43.53	-	28.23	6.77	$Na_{0.65}Mn_{0.56}Ni_{0.34}Ti_{0.10}O_{2}$
NMAT-05	23.44	40.45	1.91	27.43	6.77	$Na_{0.72}Mn_{0.52}Al_{0.05}Ni_{0.33}Ti_{0.10}O_2$
NMAT-10	24.95	36.86	3.85	26.82	7.52	Na _{0.76} Mn _{0.47} Al _{0.10} Ni _{0.32} Ti _{0.11} O ₂
NMAT-15	26.77	33.57	5.36	27.51	6.79	$Na_{0.83}Mn_{0.43}Al_{0.14}Ni_{0.33}Ti_{0.10}O_2$
NMAT-20	29.02	28.37	8.13	26.94	7.55	$Na_{0.88}Mn_{0.36}Al_{0.21}Ni_{0.32}Ti_{0.11}O_{2}$

Table S3: Comparison of specific capacity and cyclability for various layered oxide cathodes

Phase-Composition	Phase Fraction	Voltage Range vs. Na ⁺ /Na	Capacity (0.1C, mAh g ⁻¹)	Capacity retention, cycles, C rate	Ref.
Na _{0.85} Ni _{0.34} Mn _{0.33} Ti _{0.33} O ₂	P2-24.8% O3-75.2%	2.2-4.4 V	116.7	80%, 200, 1C	[1]
$Na_{0.85}Fe_{0.22}Ni_{0.33}Mn_{0.45}O_2$	P2-05% O3-95%	2.0-4.1 V	121.3	94.9%, 100, 0.2C	[2]
$Na_xLi_{0.05}Mn_{0.55}Ni_{0.3}Cu_{0.075}Mg_{0.025}O_2$	P2-32.3% O3-67.7%	2.0–4.3 V	149.9	63.5%, 1000, 10C	[3]
$Na_{2/3}Ni_{1/3}Mn_{1/3}Ti_{1/3}O_2$	P3-71% O3-29%	2.5–4.15 V	82	78%, 1000, 1C	[4]

$Na_{0.732}Ni_{0.273}Mg_{0.096}Mn_{0.63}O_{2} \\$	P2-78.4%	2.0–4.3 V	130	73.1%, 200, 1C	[5]
	O3-21.6% P2-8%				
Na _{0.75} Mn _{0.6} Ni _{0.3} Cu _{0.1} O ₂	O3-92%	1.5-4.2 V	142.4	70.8%, 300, 1C	[6]
$Na_{0.7}Mn_{0.41}Cu_{0.1}Fe_{0.1}Ti_{0.09}Ni_{0.25}Mg_{0.05}O_2$	P2-12%	2.0–4.3 V	138.7 (0.2C)	88.9%, 100, 2C	[7]
	O3-88%				
$Na_{0.8}Mn_{0.6}Ni_{0.3}Cu_{0.1}O_2$	P2-93% O3-07%	1.5–4.2 V	139	85%, 100, 0.2C 88%, 50, 0.2C	[8]
	P2-93%				
$Na_{0.8}Mn_{0.53}Fe_{0.14}Ni_{0.33}O_2$	O3-07%	2.5–4.4 V			
Na _{0.75} Mn _{0.50} Ni _{0.25} Al _{0.25} O ₂	P2-50%	2.0-4.0 V	175	82%, 300, 1C	[10]
0.75 0.50 0.25 0.25 2	P3-50%				
$Na_{0.75}Mn_{0.75}Al_{0.25}O_2$	P2-52.3%	1.5-4.2 V	150	80%, 200, 1C	[11]
	P3-47.7%				
$Na_{2/3}Ni_{1/3}Mn_{2/3}O_2$	P2-100%	1.5-4.0 V	153	40%, 100, 0.33C	[12]
No. WiMpTiO	D2 1000/	1540V	149	800/ 100 0 22C	[12]
$Na_{2/3}Ni_{1/3}Mn_{0.57}Ti_{0.10}O_2$	P2-100%	1.5-4.0 V	1 1 7	80%, 100, 0.33C	[12]
$Na_{0.77}Mn_{0.47}Al_{0.10}Ti_{0.10}Ni_{0.33}O_2$	P3-88%	1.5-4.2 V	175.5	95.5%, 50, 0.3C	This
	O3-12%				work

References

- [1] L. Yu, Z. Cheng, K. Xu, Y.-X. Chang, Y.-H. Feng, D. Si, M. Liu, P.-F. Wang, S. Xu, Interlocking biphasic chemistry for high-voltage P2/O3 sodium layered oxide cathode, Energy Storage Mater., 50 (2022) 730-739. https://doi.org/10.1016/j.ensm.2022.06.012
- [2] G. Sun, J. Guan, Y. Chen, L. Lin, X. Zhu, X. Huang, O3/P2 Biphasic Layered Cathode Material for Stable Na-Ion Storage, Energy Fuels, 39 (2025) 3338-3347. https://doi.org/10.1021/acs.energyfuels.4c05552
- [3] C. Lin, P. Dai, X. Wang, J. Sun, S. Zhuang, L. Wu, M. Lu, Y. Wen, P2/O3 biphase integration promoting the enhancement of structural stability for sodium layered oxide cathode, Chem. Eng. J., 480 (2024) 147964. https://doi.org/10.1016/j.cej.2023.147964
- [4] S.Y. Zhang, Y.J. Guo, Y.N. Zhou, X.D. Zhang, Y.B. Niu, E.H. Wang, L.B. Huang, P.F. An, J. Zhang, X.A. Yang, Y.X. Yin, S. Xu, Y.G. Guo, P3/O3 Integrated Layered Oxide as High-Power and Long-Life Cathode toward Na-Ion Batteries, Small, 17 (2021). https://doi.org/10.1002/smll.202007236
- [5] L. Zhang, C. Guan, J. Zheng, H. Li, S. Li, S. Li, Y. Lai, Z. Zhang, Rational design of intergrowth P2/O3 biphasic layered structure with reversible anionic redox chemistry and structural evolution for Na-ions batteries, Sci. Bull., 68 (2023) 180-191. https://doi.org/10.1016/j.scib.2023.01.010
- [6] J. Zhou, J. Liu, Y. Li, Z. Zhao, P. Zhou, X. Wu, X. Tang, J. Zhou, Reaching the initial coulombic efficiency and structural stability limit of P2/O3 biphasic layered cathode for sodium-ion batteries, J. Colloid Interface Sci., 638 (2023) 758-767. https://doi.org/10.1016/j.jcis.2023.02.001
- [7] J. Sun, C.-l. Liu, C.-x. Chen, F. Hua, H.-b. Huang, M.-l. Xie, L.-l. Liu, J.-t. Huang, D. Ma, X.-h. Zhang, X. Liang, A cobalt-free high-entropy P2/O3 layered oxide cathode with suppressed oxygen redox for sodium-ion batteries, J. Power Sources, 653 (2025) 237718. https://doi.org/10.1016/j.jpowsour.2025.237718
- [8] S. Saxena, H.N. Vasavan, M. Badole, A.K. Das, S. Deswal, P. Kumar, S. Kumar, Tailored P2/O3 phase-dependent electrochemical behavior of Mn-based cathode for sodium-ion batteries, J. Energy Storage, 64 (2023) 107242. https://doi.org/10.1016/j.est.2023.107242
- [9] S. Saxena, H.N. Vasavan, N. Dagar, V. Srihari, A.K. Das, P. Gami, S. Deswal, P. Kumar, H.K. Poswal, S. Kumar, Strategic phase modulation in Na_{0.8}(Mn-Fe-Ni)O₂ system delivers high energy density and structural stability, J. Power Sources, 644 (2025) 237115. https://doi.org/10.1016/j.jpowsour.2025.237115
- [10] H.N. Vasavan, M. Badole, S. Saxena, V. Srihari, A.K. Das, P. Gami, N. Dagar, S. Deswal, P. Kumar, H.K. Poswal, S. Kumar, Rational design of an optimal Al-substituted layered oxide cathode for Na-ion batteries, Electrochim. Acta, 494 (2024) 144457. https://doi.org/10.1016/j.electacta.2024.144457
- [11] H.N. Vasavan, M. Badole, S. Saxena, V. Srihari, A.K. Das, P. Gami, S. Deswal, P. Kumar, S. Kumar, Impact of P3/P2 mixed phase on the structural and electrochemical performance of Na_{0.75}Mn_{0.75}Al_{0.25}O₂ cathode, J. Energy Storage, 74 (2023) 109428. https://doi.org/10.1016/j.est.2023.109428
- [12] N. Dagar, S. Saxena, H.N. Vasavan, A.K. Das, P. Gami, S. Deswal, P. Kumar, K. Chinnathambi, V. Rathee, S. Kumar, Ti-Substitution Facilitating Anionic Redox and Cycle

Stability in a P2-Type $Na_{2/3}Mn_{2/3}Ni_{1/3}O_2$ Na-Ion Battery Cathode, Energy & Fuels, 39 (2025) 3348-3358. 10.1021/acs.energyfuels.4c05945